



# **NAVAL POSTGRADUATE SCHOOL**

**MONTEREY, CALIFORNIA**

## **THESIS**

**TIME/FREQUENCY RELATIONSHIPS FOR AN  
FFT-BASED ACOUSTIC MODEM**

by

William F. Jenkins II

September 2010

Thesis Advisor:  
Second Reader:

Joseph A. Rice  
Lawrence J. Ziomek

**Approved for public release; distribution is unlimited**

THIS PAGE INTENTIONALLY LEFT BLANK

<b>REPORT DOCUMENTATION PAGE</b>			<i>Form Approved OMB No. 0704-0188</i>	
Public reporting burden for this collection of information is estimated to average 1 hour per response, including the time for reviewing instruction, searching existing data sources, gathering and maintaining the data needed, and completing and reviewing the collection of information. Send comments regarding this burden estimate or any other aspect of this collection of information, including suggestions for reducing this burden, to Washington headquarters Services, Directorate for Information Operations and Reports, 1215 Jefferson Davis Highway, Suite 1204, Arlington, VA 22202-4302, and to the Office of Management and Budget, Paperwork Reduction Project (0704-0188) Washington DC 20503.				
<b>1. AGENCY USE ONLY (Leave blank)</b>		<b>2. REPORT DATE</b> September 2010	<b>3. REPORT TYPE AND DATES COVERED</b> Master's Thesis	
<b>4. TITLE AND SUBTITLE</b> Time/Frequency Relationships for an FFT-Based Acoustic Modem			<b>5. FUNDING NUMBERS</b>	
<b>6. AUTHOR(S)</b> William F. Jenkins II				
<b>7. PERFORMING ORGANIZATION NAME(S) AND ADDRESS(ES)</b> Naval Postgraduate School Monterey, CA 93943-5000			<b>8. PERFORMING ORGANIZATION REPORT NUMBER</b>	
<b>9. SPONSORING /MONITORING AGENCY NAME(S) AND ADDRESS(ES)</b> N/A			<b>10. SPONSORING/MONITORING AGENCY REPORT NUMBER</b>	
<b>11. SUPPLEMENTARY NOTES</b> The views expressed in this thesis are those of the author and do not reflect the official policy or position of the Department of Defense or the U.S. Government. IRB Protocol number _____.				
<b>12a. DISTRIBUTION / AVAILABILITY STATEMENT</b> Approved for public release; distribution is unlimited.			<b>12b. DISTRIBUTION CODE</b> A	
<b>13. ABSTRACT (maximum 200 words)</b>  This thesis proposes a scheme for short-range (<500m) underwater acoustic communications in shallow water. The proposed scheme is a variation on an existing commercial modem reliably used for medium-range (<5km) communications in the 9-14 kHz band. The proposed scheme exploits a higher carrier frequency at 45 kHz and increased spectral bandwidth compatible with the short-range link, thus achieving an increased channel capacity. Analytical expressions are provided for the scheme, which combines principles of M-ary frequency-shift keying (MFSK) and orthogonal frequency-division multiplexing (OFDM) in a modulation referred to as multi-channel MFSK. The proposed scheme consists of 32 orthogonally spaced channels, each of which contains a 4-ary FSK pulse train. Existing medium-range modem algorithms are adapted for the higher carrier frequency and candidate variations are implemented with bandwidths of 10 and 20 kHz. The variations involve bandwidth scaling or multiplexing the original 5 kHz spectral bandwidth. Of concern for short-range links in shallow water is multipath interference, which causes time-spreading and significant intersymbol interference (ISI). Dominant eigenray paths are determined in order to estimate the amount of time-spread expected in various shallow water environments. These are analyzed with respect to the time/frequency relationships of multi-channel MFSK to comparatively evaluate the candidate variations in terms of protection against ISI. On this basis, we propose multiplexing the 5 kHz MFSK modulation across the larger operating band.				
<b>14. SUBJECT TERMS</b> Acoustics, sound, ocean, acoustic communications, underwater networks, LAN, Seaweb, Seastar, frequency-shift keying, MFSK, multipath propagation, intersymbol interference			<b>15. NUMBER OF PAGES</b> 102	
			<b>16. PRICE CODE</b>	
<b>17. SECURITY CLASSIFICATION OF REPORT</b> Unclassified	<b>18. SECURITY CLASSIFICATION OF THIS PAGE</b> Unclassified	<b>19. SECURITY CLASSIFICATION OF ABSTRACT</b> Unclassified	<b>20. LIMITATION OF ABSTRACT</b> UU	

NSN 7540-01-280-5500

Standard Form 298 (Rev. 2-89)  
Prescribed by ANSI Std. Z39-18

THIS PAGE INTENTIONALLY LEFT BLANK

**Approved for public release; distribution is unlimited**

**TIME/FREQUENCY RELATIONSHIPS FOR AN FFT-BASED  
ACOUSTIC MODEM**

William F. Jenkins II  
Ensign, United States Navy  
B.S., United States Naval Academy, 2009

Submitted in partial fulfillment of the  
requirements for the degree of

**MASTER OF SCIENCE IN ENGINEERING ACOUSTICS**

from the

**NAVAL POSTGRADUATE SCHOOL  
September 2010**

Author: William F. Jenkins II

Approved by: Joseph A. Rice  
Thesis Advisor

Lawrence J. Ziomek  
Second Reader

Daphne Kapolka  
Chair, Engineering Acoustics Academic Committee

THIS PAGE INTENTIONALLY LEFT BLANK

## ABSTRACT

This thesis proposes a scheme for short-range ( $<500\text{m}$ ) underwater acoustic communications in shallow water. The proposed scheme is a variation on an existing commercial modem reliably used for medium-range ( $<5\text{km}$ ) communications in the 9-14 kHz band. The proposed scheme exploits a higher carrier frequency at 45 kHz and increased spectral bandwidth compatible with the short-range link, thus achieving an increased channel capacity. Analytical expressions are provided for the scheme, which combines principles of M-ary frequency-shift keying (MFSK) and orthogonal frequency-division multiplexing (OFDM) in a modulation referred to as multi-channel MFSK. The proposed scheme consists of 32 orthogonally spaced channels, each of which contains a 4-ary FSK pulse train. Existing medium-range modem algorithms are adapted for the higher carrier frequency and candidate variations are implemented with bandwidths of 10 and 20 kHz. The variations involve bandwidth scaling or multiplexing the original 5 kHz spectral bandwidth. Of concern for short-range links in shallow water is multipath interference, which causes time-spreading and significant intersymbol interference (ISI). Dominant eigenray paths are determined in order to estimate the amount of time-spread expected in various shallow water environments. These are analyzed with respect to the time/frequency relationships of multi-channel MFSK to comparatively evaluate the candidate variations in terms of protection against ISI. On this basis, we propose multiplexing the 5 kHz MFSK modulation across the larger operating band.

THIS PAGE INTENTIONALLY LEFT BLANK



# TABLE OF CONTENTS

<b>I.</b>	<b>INTRODUCTION.....</b>	<b>1</b>
<b>A.</b>	<b>BACKGROUND .....</b>	<b>1</b>
<b>B.</b>	<b>SCOPE .....</b>	<b>2</b>
<b>C.</b>	<b>APPROACH.....</b>	<b>2</b>
<b>II.</b>	<b>THE COMMUNICATION CHANNEL .....</b>	<b>5</b>
<b>A.</b>	<b>THE ACOUSTIC CHANNEL MODEL.....</b>	<b>6</b>
<b>B.</b>	<b>ACOUSTIC SIGNAL-TO-NOISE POWER RATIO .....</b>	<b>7</b>
1.	Signal.....	8
2.	Noise .....	8
<b>C.</b>	<b>WIDEBAND ACOUSTIC LINK BUDGET .....</b>	<b>10</b>
1.	Source Level .....	10
2.	Transmission Loss.....	12
3.	Noise Level.....	18
4.	Transmission Frequency .....	20
<b>D.</b>	<b>THE FADING CHANNEL .....</b>	<b>22</b>
1.	Multipath Spread.....	24
2.	Doppler Spread .....	24
3.	Intersymbol Interference.....	26
<b>III.</b>	<b>MULTI-CHANNEL M-ARY FREQUENCY-SHIFT KEYING .....</b>	<b>29</b>
<b>A.</b>	<b>MODULATION .....</b>	<b>29</b>
<b>B.</b>	<b>IMPLEMENTATION .....</b>	<b>37</b>
1.	Bandwidth Scaling .....	37
2.	Frequency Multiplexing .....	39
<b>IV.</b>	<b>DEMODULATION.....</b>	<b>43</b>
<b>V.</b>	<b>SIMULATIONS .....</b>	<b>45</b>
<b>A.</b>	<b>BANDWIDTH SCALING.....</b>	<b>46</b>
<b>B.</b>	<b>FREQUENCY MULTIPLEXING .....</b>	<b>51</b>
<b>VI.</b>	<b>CONCLUSIONS .....</b>	<b>57</b>
<b>A.</b>	<b>FINDINGS .....</b>	<b>57</b>
<b>B.</b>	<b>RECOMMENDATIONS FOR FUTURE WORK.....</b>	<b>58</b>
<b>APPENDIX A.</b>	<b>4-ARY FSK SIMULATION RESULTS .....</b>	<b>59</b>
<b>APPENDIX B.</b>	<b>4-ARY FSK SIMULATION CODE .....</b>	<b>69</b>
<b>APPENDIX C.</b>	<b>DESCRIPTION OF THE BELLHOP UNDERWATER ACOUSTIC PROPAGATION MODEL .....</b>	<b>73</b>
<b>APPENDIX D.</b>	<b>DATA EXTRACTION CODE.....</b>	<b>77</b>
	<b>LIST OF REFERENCES.....</b>	<b>79</b>
	<b>INITIAL DISTRIBUTION LIST .....</b>	<b>81</b>

THIS PAGE INTENTIONALLY LEFT BLANK

## LIST OF FIGURES

Figure 1.	Seastar LAN and Seaweb WAN concept.....	1
Figure 2.	The Open Systems Interconnection model. ....	3
Figure 3.	(a) Simple model of a linear, time- and space-invariant communication channel. The received signal $y(t)$ is a convolution of the transmitted signal $x(t)$ with the channel impulse response $h(t)$ . (b) The equivalent of (a) in the frequency domain. The spectrum $Y(f)$ of the received signal is the product of the transmitted signal's spectrum $X(f)$ and the channel's spectrum $H(f)$ . ....	5
Figure 4.	Source level frequency response of a high-frequency transducer. From [13].....	11
Figure 5.	Axial beam pattern of a high-frequency, omnidirectional transducer transmitting at 40 kHz. From [13] .....	12
Figure 6.	The three components of absorption. For frequencies above 10 kHz, $\text{MgSO}_4$ is the dominant contributor to absorptive losses.....	15
Figure 7.	Transmission loss as a function of range and frequency. Variation along the horizontal axis is a function of geometric spreading and absorption, whereas variation along the vertical axis is only a function of absorption. A temperature of 13°C, pH of 8.0, depth of 100 m, and salinity of 35 ppt are assumed. ....	16
Figure 8.	Noise spectrum level (NSL) for deep water as formulated by Coates [10]. A wind speed of 5 m/s and light shipping density are assumed. ....	19
Figure 9.	Transmission loss and noise level (from Coates) as a function of frequency and range.....	21
Figure 10.	Transmission loss plus noise level (from Coates) as a function of frequency at a range of 500 m for four wind speeds.....	22
Figure 11.	The upper plot is a Bellhop ray trace for a fan of 91 Gaussian beams in an iso-speed sound channel. The lower plot displays the eigenrays, or those rays that intercept a receiver at range $r = 500$ m.....	23
Figure 12.	Direct-path and surface-reflected path pulse trains for a long-range source-receiver geometry.....	27
Figure 13.	Direct-path and surface-reflected path pulse trains for a short-range source-receiver geometry.....	27
Figure 14.	Normalized power spectra for four orthogonally spaced sinc functions. The spacing between any two functions' peaks is $1/T$ , so that peaks are centered at the other functions' zero crossings. ....	32
Figure 15.	Frequency spectrum of the multi-channel MFSK waveform centered at 45 kHz, $T = 25$ ms. Shown are 32 channels (pulse trains) of 4-ary FSK.....	35
Figure 16.	Frequency-division multiplexing of the MFSK channels (pulse trains) produces the multi-channel MFSK waveform $x(t)$ . ....	36
Figure 17.	Spectrogram of the multi-channel MFSK signal used in Seaweb. The abscissa is time, and the ordinate is frequency. ....	37

Figure 18.	Frequency spectrum of the bandwidth-scaled multi-channel MFSK waveform centered at 45 kHz, $T = 12.5$ ms. Shown are 32 channels of 4-ary FSK. ....	38
Figure 19.	Frequency spectrum of the frequency-multiplexed multi-channel MFSK waveform centered at 45 kHz, $T = 25$ ms. Shown are 4 bands of 32 channels of 4-ary FSK. ....	41
Figure 20.	Theoretical BER for 4-ary FSK with no FEC in a channel with added white Gaussian noise [22]. ....	44
Figure 21.	The percentage of encoded symbols received in error are shown for the pulse durations associated with bandwidth scaling at a source-receiver depth of $z = 5$ m and for ranges between 50 and 70 m. ....	47
Figure 22.	Normalized time difference of arrival between the direct path and next multipath arrivals for a signal with a pulse duration of 6.25 ms. ....	49
Figure 23.	Normalized time difference of arrival between the direct path and next multipath arrivals for a signal with a pulse duration of 12.5 ms. ....	50
Figure 24.	Difference in SPL between the direct-path signal and the next multipath. ....	51
Figure 25.	The percentage of encoded symbols received in error are shown for the pulse durations associated with frequency multiplexing at a source-receiver depth of $z = 5$ m and for ranges between 50 and 70 m. ....	52
Figure 26.	Normalized time difference of arrival between the direct-path and next multipath arrivals for a signal with a pulse duration of 25 ms. ....	53
Figure 27.	Normalized time difference of arrival between the direct-path and next multipath arrivals for a signal with a pulse duration of 50 ms. ....	54
Figure 28.	The percentage of encoded symbols received in error are shown for all four pulse durations at a source-receiver depth of $z = 5$ m and for ranges between 50 and 70 m. ....	55
Figure 29.	The input $\text{SNR}_a$ and percentage of encoded symbols in error between 50 and 500 m for a signal with $T = 6.25$ ms and a source and receiver located at $z = 5$ m. ....	59
Figure 30.	The input $\text{SNR}_a$ and percentage of encoded symbols in error between 50 and 500 m for a signal with $T = 6.25$ ms and a source and receiver located at $z = 50$ m. ....	59
Figure 31.	The input $\text{SNR}_a$ and percentage of encoded symbols in error between 50 and 500 m for a signal with $T = 6.25$ ms and a source and receiver located at $z = 100$ m. ....	60
Figure 32.	The input $\text{SNR}_a$ and percentage of encoded symbols in error between 50 and 500 m for a signal with $T = 6.25$ ms and a source and receiver located at $z = 150$ m. ....	60
Figure 33.	The input $\text{SNR}_a$ and percentage of encoded symbols in error between 50 and 500 m for a signal with $T = 6.25$ ms and a source and receiver located at $z = 200$ m. ....	61
Figure 34.	The input $\text{SNR}_a$ and percentage of encoded symbols in error between 50 and 500 m for a signal with $T = 12.5$ ms and a source and receiver located at $z = 5$ m. ....	61

Figure 35.	The input $\text{SNR}_a$ and percentage of encoded symbols in error between 50 and 500 m for a signal with $T = 12.5$ ms and a source and receiver located at $z = 50$ m.....	62
Figure 36.	The input $\text{SNR}_a$ and percentage of encoded symbols in error between 50 and 500 m for a signal with $T = 12.5$ ms and a source and receiver located at $z = 100$ m.....	62
Figure 37.	The input $\text{SNR}_a$ and percentage of encoded symbols in error between 50 and 500 m for a signal with $T = 12.5$ ms and a source and receiver located at $z = 150$ m.....	63
Figure 38.	The input $\text{SNR}_a$ and percentage of encoded symbols in error between 50 and 500 m for a signal with $T = 12.5$ ms and a source and receiver located at $z = 200$ m.....	63
Figure 39.	The input $\text{SNR}_a$ and percentage of encoded symbols in error between 50 and 500 m for a signal with $T = 25$ ms and a source and receiver located at $z = 5$ m.....	64
Figure 40.	The input $\text{SNR}_a$ and percentage of encoded symbols in error between 50 and 500 m for a signal with $T = 25$ ms and a source and receiver located at $z = 50$ m.....	64
Figure 41.	The input $\text{SNR}_a$ and percentage of encoded symbols in error between 50 and 500 m for a signal with $T = 25$ ms and a source and receiver located at $z = 100$ m.....	65
Figure 42.	The input $\text{SNR}_a$ and percentage of encoded symbols in error between 50 and 500 m for a signal with $T = 25$ ms and a source and receiver located at $z = 150$ m.....	65
Figure 43.	The input $\text{SNR}_a$ and percentage of encoded symbols in error between 50 and 500 m for a signal with $T = 25$ ms and a source and receiver located at $z = 200$ m.....	66
Figure 44.	The input $\text{SNR}_a$ and percentage of encoded symbols in error between 50 and 500 m for a signal with $T = 50$ ms and a source and receiver located at $z = 5$ m.....	66
Figure 45.	The input $\text{SNR}_a$ and percentage of encoded symbols in error between 50 and 500 m for a signal with $T = 50$ ms and a source and receiver located at $z = 50$ m.....	67
Figure 46.	The input $\text{SNR}_a$ and percentage of encoded symbols in error between 50 and 500 m for a signal with $T = 50$ ms and a source and receiver located at $z = 100$ m.....	67
Figure 47.	The input $\text{SNR}_a$ and percentage of encoded symbols in error between 50 and 500 m for a signal with $T = 50$ ms and a source and receiver located at $z = 150$ m.....	68
Figure 48.	The input $\text{SNR}_a$ and percentage of encoded symbols in error between 50 and 500 m for a signal with $T = 50$ ms and a source and receiver located at $z = 200$ m.....	68

THIS PAGE INTENTIONALLY LEFT BLANK

## LIST OF TABLES

Table 1.	Environmental parameters for modeling and simulation of the underwater acoustic communications channel.....	7
Table 2.	Characteristic impedances are shown for air at 20°C, seawater, and a fluid-like bottom composed of quartz sand. From [11] .....	18
Table 3.	Transmission loss at the uppermost and lowermost carrier frequencies for a 4-ary FSK pulse train of bandwidth 640 Hz. ....	46
Table 4.	Total of encoded symbols received in error for each pulse duration at a source-receiver depth of $z = 5$ m and for ranges between 50 and 70 m.....	55

THIS PAGE INTENTIONALLY LEFT BLANK



## **LIST OF ACRONYMS AND ABBREVIATIONS**

BER – Bit Error Rate (p. 44)

DFT – Discrete Fourier Transform (p. 43)

FEC – Forward Error Correction (p. 44)

FDM – Frequency-Division Multiplexing (p. 2)

FFT – Fast Fourier Transform (p. 3)

GUI – Graphical User Interface (p. 6)

H<sub>3</sub>BO<sub>3</sub> – Boric Acid (p. 14)

ISI – Intersymbol Interference (p. 2)

LAN – Local Area Network (p. 1)

MFSK – M-ary Frequency-Shift Keying (p. 1)

MgSO<sub>4</sub> – Magnesium Sulfate (p. 14)

NL – Noise Level (p. 9)

NSL – Noise Spectrum Level (p. 19)

OFDM – Orthogonal Frequency-Division Multiplexing (p. 36)

RMS – Root-Mean-Square (p. 6)

SER – Symbol Error Rate (p. 3)

SNR – Signal-to-Noise Power Ratio (p. 7)

SL – Source Level (p. 9)

SPL – Sound Pressure Level (p. 50)

SSP – Sound-Speed Profile (p. 6)

TL – Transmission Loss (p. 9)

UUV – Unmanned Underwater Vehicle (p. 1)

WAN – Wide Area Network (p. 1)

THIS PAGE INTENTIONALLY LEFT BLANK

## ACKNOWLEDGMENTS

I would like to thank the following people for their support and encouragement during my time in Monterey:

First and foremost, to my parents and family, for instilling in me from a very young age the desire to never cease learning. Your constant encouragement and nurturing has served as a foundation for everything I have accomplished, and I have you to thank for helping me develop a strong drive for scientific investigation.

To Joseph Rice, who has been a constant source of encouragement and guidance over the last year. With his vast experience in underwater acoustic networking, his confidence in me motivated and enabled me to overcome many obstacles.

To Lawrence Ziomek, for the generous amounts of time he spent helping me understand the intricacies of digital communication. His knowledge and help brought a level of rigor to this thesis, which, without him, would have been impossible to achieve.

To Dale Green, for his enthusiasm and willingness to share his expertise about underwater networking. The technical advice and knowledge he shared was invaluable to the completion of this work.

To the various professors at the Naval Postgraduate School, for their passion and dedication to teaching and research. I would specifically like to thank Chad Spooner for his technical advice in developing the software models used in this thesis.

To MAJ Meng Chong Goh, Republic of Singapore Navy, and LTJG Pongsakorn Sommai, Royal Thai Navy, for their help and collaboration in understanding the Seastar network concept and prototype modems.

To the Office of Naval Research, which has sponsored the development of the Seastar concept.

And finally, to the friends I have met while in Monterey, especially from the oceanography program, who were kind enough to take a fresh ensign under their wings.

THIS PAGE INTENTIONALLY LEFT BLANK

# I. INTRODUCTION

## A. BACKGROUND

The development of Seastar, an underwater acoustic local-area network (LAN), is enabling short-range (50-500 meters), high-frequency (35-55 kHz) networked communications [1]. Seastar uses a basic star topology in which a set of peripheral nodes (sensors, divers, UUVs, platforms, etc.) transmit data to a central node for processing. The central node can also communicate with a wide-area network (WAN), such as Seaweb, an underwater acoustic WAN [2-4], for dissemination of processed data. The deployment of Seastar with Seaweb, depicted in Figure 1, allows for multiple clusters of nodes, each with its own central node, and each forming its own separate LAN, to add an additional tier of networked communications within the greater Seaweb WAN topology.

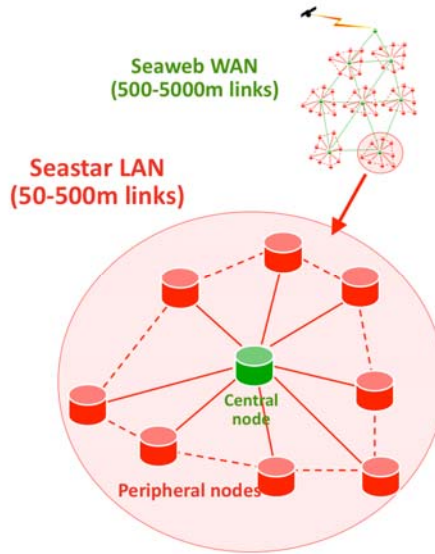


Figure 1. Seastar LAN and Seaweb WAN concept.

Currently, Seastar modems use the same modulation scheme that has been optimized for Seaweb modems, despite operating in a completely different frequency band (Seaweb operates in the 9-14 kHz band). The Seaweb scheme, a form of M-ary frequency-shift keying (MFSK) called multi-channel MFSK, has been proven to perform robustly in a variety of channel conditions [5].

In June 2007, available Seaweb modems were configured as a prototype Seastar network and deployed in St. Andrew's Bay, Florida [4]. The goal of this sea testing was to observe the effects of natural and man-made noise on network performance in a shallow water environment. The results of this testing yielded favorable results, though the prototype operated at the 9-14 kHz band rather than the envisioned 35-55 kHz Seastar operating band. Nevertheless, due to the success of the prototype testing, we now seek to design candidate variations of multi-channel MFSK that could be used aboard the high-frequency Seastar teleseismic modems in future Seastar implementations.

## **B. SCOPE**

The scope of this research includes a mathematical description of the multi-channel MFSK modulation scheme currently used aboard the Seaweb and Seastar modems. Multi-channel MFSK combines principles of traditional MFSK as well as frequency-division multiplexing (FDM). Simulation results of several candidate implementations of multi-channel MFSK are presented.

This thesis examines alternative methods by which to improve the reliability of Seastar by tuning its communication scheme for the 35-55 kHz band. The primary concern of this research is to evaluate for the various candidate modulation schemes the effects of intersymbol interference (ISI), in an effort to improve the reliability of short-range, high-frequency underwater acoustic communications.

## **C. APPROACH**

Underwater acoustic communication draws upon a wide base of knowledge involving physics, acoustics, electrical engineering, digital communications theory, and computer network theory. The multi-disciplinary field brings together academicians, scientists, engineers, and users from a wide variety of backgrounds and industries, both civilian and military. When discussing communications systems, it is often useful to place the discussion in the context of the Open Systems Interconnection reference model, shown in Figure 2. The simulations and analyses conducted in this thesis will be restricted to the physical layer, which includes modulation, transmission, channel effects,

reception and demodulation. Unique to this form of communication, it is necessary to discuss principles of underwater acoustics as the basis for the physical layer.



Figure 2. The Open Systems Interconnection model.

Chapter II describes acoustic modeling of the underwater transmission channel and quantifies fundamental characteristics of underwater acoustic propagation as they relate to digital communications. A wideband acoustic link budget analysis is presented for the 35-55 kHz band of frequencies in which Seastar is designed to operate.

Chapter III contains a mathematical representation of the multi-channel MFSK modulation scheme, providing additional equations for bandwidth scaling and frequency multiplexing.

Chapter IV describes reception of the multi-channel MFSK signal using fast Fourier transform (FFT) based demodulation. Performance in a noisy channel is characterized in the form of a symbol error rate (SER) curve for the FFT-based demodulation.

Chapter V contains channel simulations evaluating the performance of various implementations of multi-channel MFSK in various channel geometries. Error analysis is presented with attention to ISI.

Chapter VI summarizes our findings and recommends implementing a specific variation of multi-channel MFSK for use in the Seastar LAN.

THIS PAGE INTENTIONALLY LEFT BLANK



## II. THE COMMUNICATION CHANNEL

Figure 3 shows a simple model for the transmission of a signal  $x(t)$  through a linear, time- and space-invariant channel with impulse response  $h(t)$ . From basic communication theory, we know the received signal  $y(t)$  is simply a convolution of  $x(t)$  with  $h(t)$  [6].

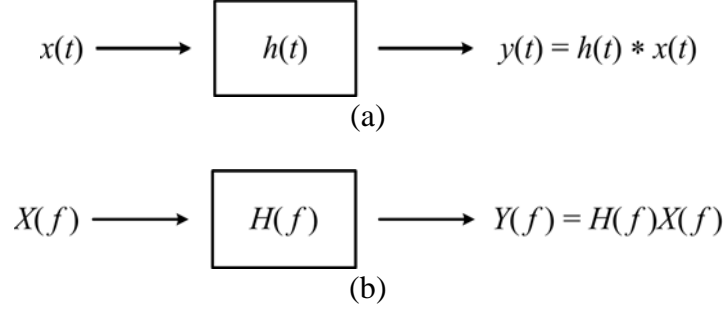


Figure 3. (a) Simple model of a linear, time- and space-invariant communication channel. The received signal  $y(t)$  is a convolution of the transmitted signal  $x(t)$  with the channel impulse response  $h(t)$ . (b) The equivalent of (a) in the frequency domain. The spectrum  $Y(f)$  of the received signal is the product of the transmitted signal's spectrum  $X(f)$  and the channel's spectrum  $H(f)$ .

With the advent of underwater acoustic digital communications, the ocean medium has increasingly been treated as a communication channel characterized by its impulse response. Because transmission loss of sound propagating through the ocean is highly dependent on frequency, a broadband signal with a flat transmitted spectrum will be received as a signal that is by no means flat. The signal may also become spread in time and frequency, and can experience phase shifts. Thus, in the context of a communication channel, the ocean may be treated as a wideband, linear, time- and space-variant, distorting filter. Attempts to find an analytic expression for the impulse response of such a channel have proven extremely difficult because of the time- and space-variant nature of the ocean [7]. Consequently, we simplify the channel by treating it as time- and space-invariant.

The frequency dependence of sound propagation has a direct impact on communications parameters like source-receiver range, transmission frequency, and bandwidth. As a result, it is imperative to characterize and account for the sources of

transmission loss in the underwater acoustic communication channel, and to identify optimal transmission parameters that ultimately assure successful demodulation of the transmitted signal. In this chapter, we describe the acoustic channel modeling software used to determine the multipath arrival characteristics of the channel, and we review principles of sound propagation in a fading acoustic communication channel.

## **A. THE ACOUSTIC CHANNEL MODEL**

We model the underwater acoustic communication channel using the Bellhop Gaussian beam tracing propagation model. The model, developed in 1987 by Porter and Buckner at the Space and Naval Warfare Systems Center in San Diego, has since been migrated into a MATLAB graphical user interface (GUI) available from the Centre for Marine Science and Technology at the Curtin University of Technology at Perth, Australia [8]. The interface allows users to model multiple layers of water and sediment, each with its own set of unique environmental parameters, such as the sound-speed profile (SSP), density, and root-mean-square (RMS) roughness. The model is capable of producing channel impulse responses, ray traces, source-to-receiver eigenrays, and two-dimensional transmission loss plots. The version of Bellhop used for this research is coupled to a bottom-loss model called Bounce [8]. From this point forward, we refer to the model as the Bellhop model. Further information about the Bellhop model is given in Appendix C.

In order to more clearly illustrate the time/frequency relationships for the various candidate modulation schemes, we model propagation in a more simplified environment than would be found in nature. We define the simplified environment to consist of a homogeneous half-space of seawater with an isospeed SSP of 1500 m/s, extending from the sea surface to a depth of 205 m. The bottom half-space is assumed to be a fluid-like stratum consisting of quartz sand and extending to a 500 m depth below the sea surface. These and additional parameters are included in Table 1.

Parameter	Value
Depth	205 m
Range	50 – 500 m
Bottom Type	Quartz sand
Compressional Sound Speed (Water)	1500 m/s
Compressional Sound Speed (Bottom)	1730 m/s
Density (Water)	1026 kg/m <sup>3</sup>
Density (Bottom)	2070 kg/m <sup>3</sup>
Surface RMS Roughness	0 m
Bottom RMS Roughness	0 m
Shear Sound Speed	0 m/s
Compressional Absorption	0 dB/m
Shear Absorption	0 dB/m

Table 1. Environmental parameters for modeling and simulation of the underwater acoustic communications channel.

Because Bellhop uses Gaussian beams to model propagation, there is some error associated with the estimation of eigenrays. This error is evident in Figure 11, where the eigenrays are clearly not intercepting the receiver exactly. Because of the high-frequency, short-wavelength nature of the Seastar signals, this error could significantly impact the phases of the received eigenrays, though to what extent is unknown and should be examined in follow-on work.

## B. ACOUSTIC SIGNAL-TO-NOISE POWER RATIO

One of the most important measures for evaluating communications performance is the signal-to-noise power ratio (SNR). Because SNR is often defined inconsistently between the technical communications community and the underwater acoustics community, we present a definition of the acoustic signal-to-noise power ratio in generally accepted acoustic terms. This particular treatment of SNR is developed more extensively in [4]. The acoustic signal-to-noise power ratio  $\text{SNR}_a$  is presented as follows:

$$\text{SNR}_a \equiv \frac{E\left\{|p_s(t, \mathbf{r}_1)|^2\right\}}{E\left\{|p_n(t, \mathbf{r}_1)|^2\right\}} \quad (2.1)$$

where  $E\{\bullet\}$  is the expected value or first moment, and  $p_s(t, \mathbf{r}_1)$  and  $p_n(t, \mathbf{r}_1)$  are the acoustic pressures of the signal and noise, respectively, incident at a receiver located at

$\mathbf{r}_1 = x_1 \hat{i} + y_1 \hat{j} + z_1 \hat{k}$ .  $\text{SNR}_a$  quantifies the strength of the received signal compared to the received noise before processing occurs, and is a useful measurement since it is indicative of the communications performance that may be expected.

## 1. Signal

The multi-channel MSFK communication signals used in the Seaweb and Seastar underwater networks are composed of a band of frequencies. Because each frequency experiences a varying amount of transmission loss, it is necessary to express the numerator in (2.1) in terms of a narrowband frequency component. Consider a stationary, omnidirectional, time-harmonic point source located at  $\mathbf{r}_0 = x_0 \hat{i} + y_0 \hat{j} + z_0 \hat{k}$  transmitting a signal. The magnitude of the signal's acoustic pressure incident on the receiver located at  $\mathbf{r}_1$  can be given by:

$$|p_s(t, \mathbf{r}_1)| = P_0 \frac{R}{r_{0,1}} e^{-\alpha(f)(r_{0,1}-R)} \quad (2.2)$$

where  $P_0$  is the acoustic pressure amplitude of the signal at the source in micropascals ( $\mu\text{Pa}$ ),  $R$  is the reference range from the source,  $r_{0,1}$  is the range between the source and receiver in meters, and  $\alpha(f)$  is the frequency-dependent attenuation coefficient in nepers per meter (Np/m). Spherical spreading of the propagating wave front is assumed. It is shown in [4] that for a time-harmonic acoustic pressure at time  $t$  seconds and at location  $\mathbf{r}_1$ , the average power of the signal may be expressed as:

$$E\{|p_s(t, \mathbf{r}_1)|^2\} = \langle |p_s(t, \mathbf{r}_1)|^2 \rangle = \left( \frac{\sqrt{2}}{2} P_0 \frac{R}{r_{0,1}} \right)^2 e^{-2\alpha(f)(r_{0,1}-R)} = p_{rms,s}^2(\mathbf{r}_1) \quad (2.3)$$

where  $p_{rms,s}(\mathbf{r}_1)$  is the RMS value of the acoustic pressure of the signal at the receiver.

## 2. Noise

Noise in the underwater communications channel originates from a variety of sources, with major contributions from shipping, wind, hydrodynamics, seismic activity, and biologics [9, 10]. If we treat  $p_n(t, \mathbf{r}_1)$  as a zero-mean, wide-sense-stationary, random,

Gaussian process that is an arbitrary function of time, it can be shown [4] that the average power of the noise incident at the receiver is:

$$E\left\{\left|p_n(t, \mathbf{r}_1)\right|^2\right\} = \sigma_{p_n}^2(\mathbf{r}_1) = 2S_{p_n}(f, \mathbf{r}_1)\Delta f \quad (2.4)$$

where  $\sigma_{p_n}^2(\mathbf{r}_1)$  is the variance of the noise,  $S_{p_n}(f, \mathbf{r}_1)$  is the power spectral density function in  $\text{Pa}^2/\text{Hz}$ , and  $\Delta f$  is a limited noise bandwidth, generally taken to be 1 Hz. Substituting (2.3) and (2.4) into (2.1) yields:

$$\text{SNR}_a = \frac{p_{ms,s}^2(\mathbf{r}_1)}{\sigma_{p_n}^2(\mathbf{r}_1)} = \frac{\left(\frac{\sqrt{2}}{2}P_0\frac{R}{r_{0,1}}\right)^2}{2S_{p_n}(f, \mathbf{r}_1)\Delta f} e^{-2\alpha(f)(r_{0,1}-R)} \quad (2.5)$$

A more useful form of (2.5) is attained by expressing the  $\text{SNR}_a$  in terms of sound pressure levels relative to a reference acoustic pressure  $P_{ref}$ , resulting in the familiar passive sonar equation terms of source level (SL), noise level (NL), and transmission loss (TL):

$$\text{SNR}_a(\text{dB}) = \text{SL} - (\text{NL} + \text{TL}) \quad (2.6)$$

where

$$\text{SNR}_a(\text{dB}) = 10\log(\text{SNR}_a) \quad (2.7)$$

$$\text{SL} = 20\log\left(\frac{\frac{\sqrt{2}}{2}P_0}{P_{ref}}\right) \text{ dB re } P_{ref} \quad (2.8)$$

$$\text{NL} = 10\log\left(\frac{2S_{p_n}(f, \mathbf{r}_1)}{P_{ref}^2}\right) \text{ dB re } P_{ref}^2 \quad (2.9)$$

$$\text{TL} = 20\log(r_{0,1}) + \alpha'(f)(r_{0,1}-1) \text{ dB} \quad (2.10)$$

and  $\alpha'(f) = 8.686\alpha(f)$ , where  $\alpha'(f)$  is in dB/m [11]. In (2.8) – (2.10),  $R = 1$  m,  $\Delta f = 1$  Hz, and for underwater acoustics,  $P_{ref} = 1$   $\mu\text{Pa}$ .

We next seek to describe acoustically what affects values for source level, noise level, and transmission loss in the context of (2.6). It is worth emphasizing that each of the terms in (2.6) is frequency dependent. Thus, the acoustic SNR given by (2.6), when expressed as a function of frequency, can represent effects of the channel on a signal at a

certain frequency. As covered in a subsequent section, it is therefore possible to find the optimal transmission frequency for a desired communication range given a set of environmental conditions.

## C. WIDEBAND ACOUSTIC LINK BUDGET

The wideband acoustic link budget is a method by which  $\text{SNR}_a$  may be calculated using (2.6) [12]. Each term in (2.6) and its dependence on frequency is discussed in the subsequent sections.

### 1. Source Level

The source level of an omnidirectional transmitter may be defined as [11]:

$$\text{SL} = 10 \log \left( \frac{I_{\text{source@1m}}}{I_{\text{ref}}} \right) \text{ dB} \quad (2.11)$$

where  $I_{\text{source@1m}}$  is the acoustic intensity of the transmitted signal referenced at one meter from the transmitter, and  $I_{\text{ref}}$  is a standard reference intensity. The general equation for acoustic intensity is given by:

$$I = \frac{\Pi}{A} \text{ W/m}^2 \quad (2.12)$$

where  $\Pi$  is the acoustic power and  $A$  is the surface area surrounding the acoustic center. At a radius of one meter, the transmitter is surrounded by a sphere of surface area:

$$A = 4\pi r^2 = 4\pi \text{ m}^2 \quad (2.13)$$

Substituting (2.13) into (2.12) for  $I_{\text{source@1m}}$  yields:

$$I_{\text{source@1m}} = \frac{\Pi}{4\pi} \text{ W/m}^2 \quad (2.14)$$

The standard reference pressure for underwater acoustics is 1  $\mu\text{Pa}$ , which is equivalent to a reference intensity of  $0.67 \times 10^{-18} \text{ W/m}^2$  [11]. Substituting this value and (2.14) into (2.11), we obtain:

$$\begin{aligned} \text{SL} &= 10 \log \left( \frac{\frac{\Pi}{4\pi} \text{ W/m}^2}{0.67 \times 10^{-18} \text{ W/m}^2} \right) \text{ dB re } 1 \mu\text{Pa @ } 1 \text{ m} \\ &= 10 \log(\Pi) + 170.7 \text{ dB re } 1 \mu\text{Pa @ } 1 \text{ m} \end{aligned} \quad (2.15)$$

For example, if we assume  $\Pi$  is 1 W, then the source level is simply 170.7 dB re 1  $\mu\text{Pa}$  @ 1 m.

An important consideration for acoustic communications is the proper selection of the source level. On the one hand, it is important to set the source level high enough so that the received energy is higher than the receiver's detection threshold. On the other hand, if the source level is set too high, the channel reverberation will be very strong, prolonging the channel's impulse response by elevating weak multipath returns above the background noise. Achieving a high SNR—which is desirable for the direct path signal—by increasing source level, also makes multipath returns stronger, which can degrade receiver performance.

In addition to selecting a source level, it is necessary to examine how the source level changes with frequency. Building a transducer with a flat frequency response across the range of transmission frequencies is very difficult and rarely achieved, so it is necessary to measure the frequency response of the transducer being used. With the frequency response known, the modulator can compensate for any deviations from the desired response by equalizing the amplitude of the signal at particular frequencies. Figure 4 shows the frequency response of the source level of a spherical transducer used aboard a prototype Seastar high-frequency acoustic modem.

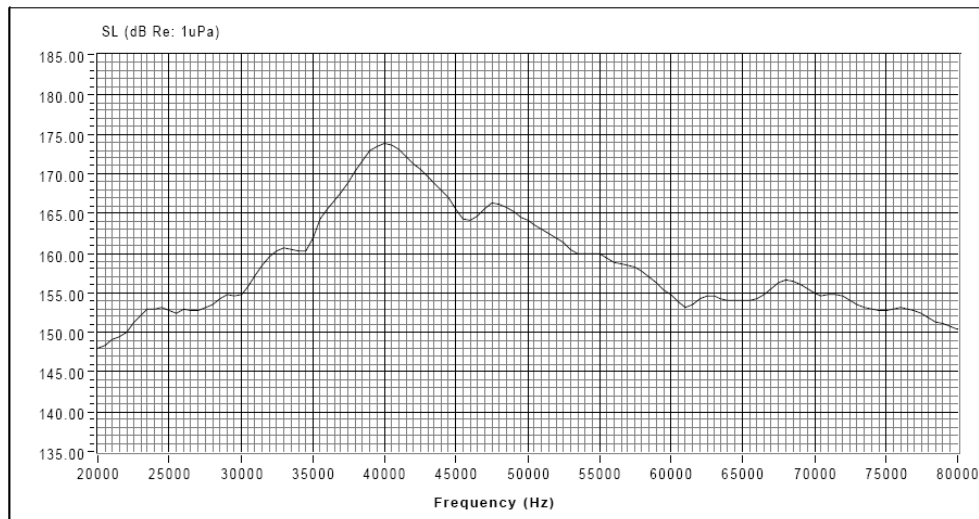


Figure 4. Source level frequency response of a high-frequency transducer. From [13]

Source level is further dependent on the directionality of the transducer. Ideally, an omnidirectional source radiates acoustic pressure uniformly in all directions. However, source levels can vary greatly with direction, as illustrated by Figure 5, which shows the axial beam pattern of the same transducer as that measured in Figure 4.

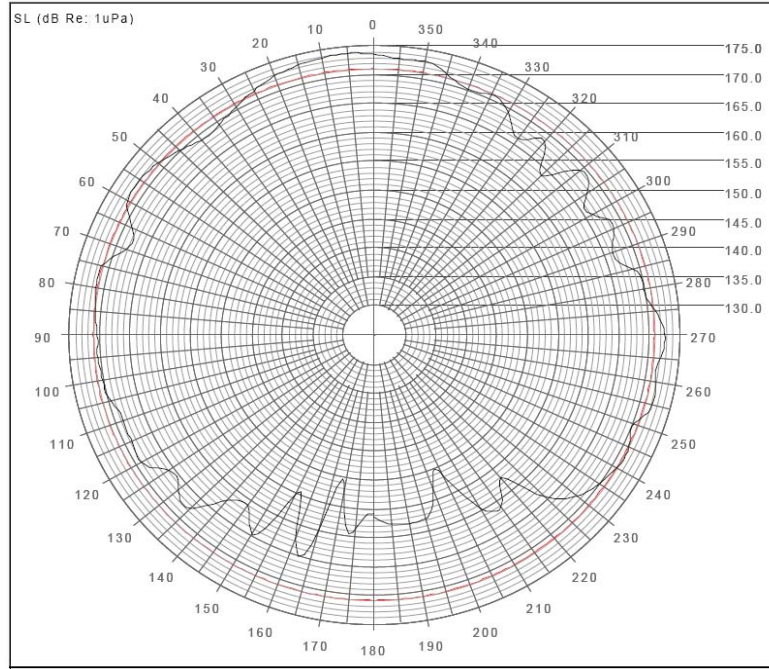


Figure 5. Axial beam pattern of a high-frequency, omnidirectional transducer transmitting at 40 kHz. From [13]

Another important consideration for source level is the material condition of the transducer [14]. All transducers are subject to degradation caused by material and electrical stresses and strains incurred during the conversion of electrical energy into or from mechanical energy. Higher source levels induce greater forces that act on the transducer and, if overdriven, can shorten its life or permanently damage it.

## 2. Transmission Loss

Transmission loss is a quantitative description of the weakening of an acoustic signal between two points. It is most often expressed as a logarithmic ratio between the sound intensity  $I_0$  at a point one meter from the acoustic center of the source, and the sound intensity  $I_1$  at some distant point [11]. Equation (2.16) gives the transmission loss in decibels:



$$TL = 10 \log \left( \frac{I_0}{I_1} \right) \text{ dB} \quad (2.16)$$

There are a variety of methods by which transmission loss is obtained, some resulting from physical theory and others from empirical observation and experimentation. Nevertheless, transmission loss between two points is fundamentally dependent on two broad categories of losses: geometric and nongeometric. Geometric losses occur as a result of expansion of the acoustic wave front during propagation. Nongeometric losses occur as a result of absorption, scattering, leakage, and other factors, and tend to be highly dependent on environmental conditions.

Because only a rough estimate of transmission loss was desired for this thesis, the geometric spreading of the shallow channel was estimated by using simple cylindrical spreading. The transmission loss formula for cylindrical spreading can be derived as follows. Between an upper plane located at the surface, at  $z = 0$  m, and a lower plane located at the bottom, at a depth of  $z = H$  m, energy is conserved and the radiated acoustic power,  $\Pi$ , is constant regardless of range  $r$ . When the wave front begins interacting with the parallel plane boundaries, it begins to spread cylindrically outward. Because the acoustic power is the product of acoustic intensity and the area of the wave front, and since the power remains constant regardless of range, the acoustic power of a cylindrically spreading wave front may be written as:

$$\Pi = 2\pi r_0 H I_0 = 2\pi r_1 H I_1 \quad (2.17)$$

Solving for the intensities yields:

$$I_0 = \frac{\Pi}{2\pi r_0 H} \quad (2.18)$$

$$I_1 = \frac{\Pi}{2\pi r_1 H} \quad (2.19)$$

Applying the convention  $r_0 = 1$  m, and substituting (2.18) and (2.19) into (2.16), the cylindrical transmission loss is:

$$TL_{cyl} = 10 \log r_1 \text{ dB} \quad (2.20)$$

One of the nongeometric sources of transmission loss is absorption [9, 11]. The contribution of absorption to transmission loss is a function of range, among other variables:

$$TL_{abs} = \alpha r \text{ dB} \quad (2.21)$$

There have been several theoretical and empirical attempts to quantify  $\alpha$ , which is the absorption coefficient at frequency  $f$ . Fisher and Simmons developed one of the most well known equations for  $\alpha$  [16]; however, Francois and Garrison further refined the equation through extensive measurements, so we use their equation to model absorptive losses [17, 18]:

$$\alpha = \frac{A_1 P_1 f_1 f^2}{f_1^2 + f^2} + \frac{A_2 P_2 f_2 f^2}{f_2^2 + f^2} + A_3 P_3 f^2 \text{ dB/km} \quad (2.22)$$

The absorption coefficient has three components: the first two are chemical relaxations for boric acid ( $H_3BO_3$ ) and magnesium sulfate ( $MgSO_4$ ), respectively, and the third is the contribution of pure water. The degree to which each component contributes to the absorption of sound in seawater depends on frequency  $f$ , in kHz, temperature  $T$ , in degrees Celsius, salinity  $S$ , in parts per thousand (ppt), acidity, measured by pH, and depth  $D$ , in meters. The constants also take into account sound speed as a function of temperature, salinity and depth, but for simplification and consistency, the sound speed is taken to be 1500 m/s.

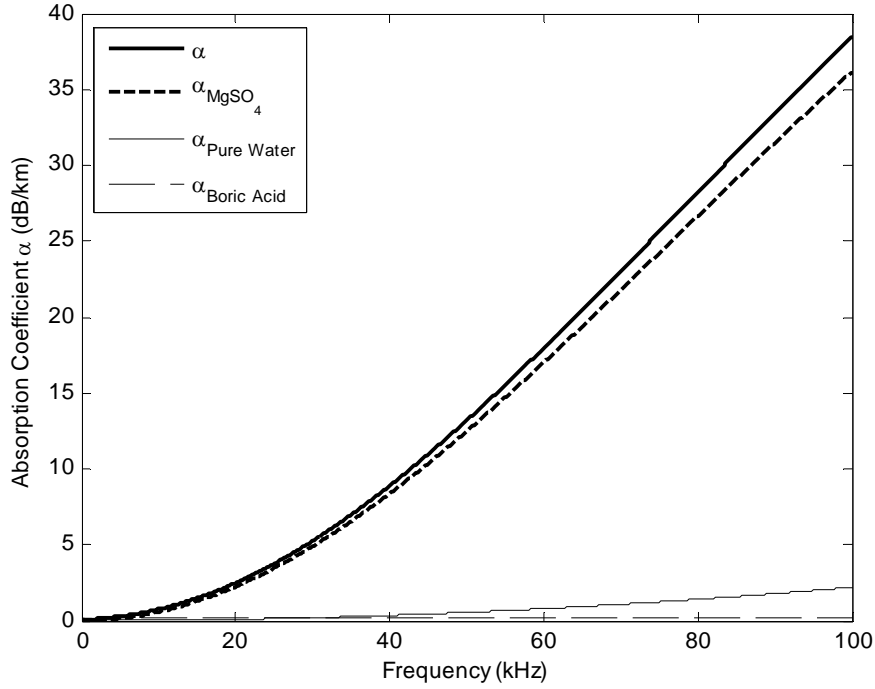


Figure 6. The three components of absorption. For frequencies above 10 kHz,  $MgSO_4$  is the dominant contributor to absorptive losses.

The contribution of each component is presented in Figure 6 for frequencies up to 100 kHz. Above 10 kHz,  $MgSO_4$  is the dominant contributor to absorption, as determined by Francois and Garrison. Thus, in the Seastar operating band of 35-55 kHz, the influences of boric acid and pure water on absorption are relatively small. At 55 kHz, the total absorption coefficient is 15.5 dB/km, and the combined effects of boric acid and pure water account for less than 1 dB/km of that loss.

The combination of (2.20) and (2.21) yields the total transmission loss in the channel due to cylindrical spreading and absorption:

$$TL = TL_{cyl} + TL_{abs} \text{ dB} \quad (2.23)$$

Figure 7 illustrates the dependence of the overall transmission loss on range and frequency. At a transmission frequency of 45 kHz, a signal experiences approximately 32 dB of transmission loss at a range of 500 m. It is readily apparent that high-frequency underwater acoustic communications are limited by transmission loss, and must therefore be restricted to short ranges.

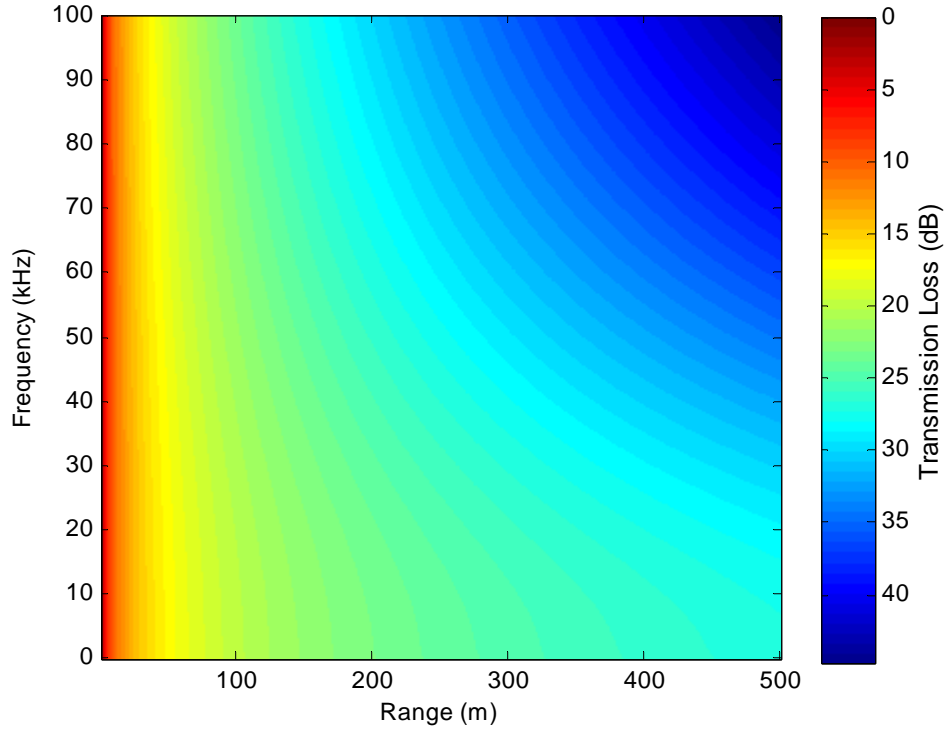


Figure 7. Transmission loss as a function of range and frequency. Variation along the horizontal axis is a function of geometric spreading and absorption, whereas variation along the vertical axis is only a function of absorption. A temperature of 13°C, pH of 8.0, depth of 100 m, and salinity of 35 ppt are assumed.

An additional contribution to transmission loss arises from interaction with the boundaries of the channel. Typical boundaries are the surface and the bottom, but may also include water layers in extremely stratified environments. The resulting transmission loss from these interactions differs greatly depending on the boundary characteristics, grazing angle of the incident acoustic waves, and acoustic frequency. For purposes of channel simulation, the specularly reflecting pressure release model of the surface, which we shall call the perfect reflector, is used for simplification. More realistically, however, the sea surface is modulated by a field of gravity waves resulting from a variety of air-sea forcing mechanisms, such as wind, and can exhibit a diversity of statistical characteristics. With regard to transmission loss, when an acoustic ray interacts with a rough surface, scattering can occur as a result of diffuse reflection. The degree of scattering is dependent on the roughness of the surface and the wavelength of the acoustic

wave [9, 19]. For a surface that is flat over a few wavelengths of the sound, the acoustic wave is specularly reflected, and its propagation may be modeled readily as an unscattered ray. For a surface whose variations occur on the order of one wavelength of the sound, the wave is scattered due to diffuse reflection. For surface variations smaller than one wavelength of the sound, the propagation of the diffuse reflection approaches that of a spherical wave as the volume of the surface variation approaches the limit of zero [19]. The overall degree of scattering of an acoustic wave may be quantified by the Rayleigh parameter [9]:

$$R = kh \sin(\theta) \quad (2.24)$$

where  $k = 2\pi/\lambda \text{ m}^{-1}$  is the wave number,  $H$  is the surface wave height in meters, and  $\theta$  is the grazing angle of the ray. For  $R \gg 1$ , the surface acts as a scatterer, and for  $R \ll 1$ , the surface acts as a reflector [9]. Thus, for a given surface roughness, acoustic signals with smaller wavelengths, and therefore higher frequencies, are more susceptible to scattering as a result of diffuse reflection than lower frequency signals. Additionally, the statistical characteristics of the scattered acoustic signals will be dependent on those of the surface. We neglect scattering in order to simplify the channel model, and because the method by which Bellhop accounts for scattering was not investigated.

Treating the surface as a perfect reflector is justified by the large characteristic acoustic impedance mismatch between seawater and air, which happens to be four orders of magnitude as seen in Table 2. However, the characteristic acoustic impedances of seawater and a fluid-like bottom, such as quartz sand, are of the same order of magnitude. Thus, when sound waves interact with the bottom, in addition to experiencing scattering, energy is lost to propagation into the bottom half-space. This loss of energy is termed energy leakage, since the acoustic energy that propagates and is absorbed into the bottom medium is ultimately lost from the communication channel. As a result, every time a ray interacts with the bottom, a quantifiable amount of energy is lost and may be modeled as transmission loss inherent to that particular ray. For multipath propagation, each ray has a unique amplitude dependent not only on the factors previously discussed, but also on the number of surface reflections and bottom bounces it experiences throughout its

propagation path. The Bellhop acoustic model couples acoustic ray tracing with bottom bounce transmission loss, yielding an associated amplitude for each ray, making it an appropriate tool for multipath propagation analysis.

<b>Characteristic Acoustic Impedance <math>\rho_0 c</math> (Pa·s/m)</b>	
Air	415
Water (sea)	$1.54 \times 10^6$
Quartz Sand	$3.58 \times 10^6$

Table 2. Characteristic impedances are shown for air at 20°C, seawater, and a fluid-like bottom composed of quartz sand. From [11]

The channel simulations presented in Chapter V assume a homogeneous layer of seawater and a bottom half-space. It is worth noting that Bellhop can model several layers, each with its own unique environmental properties such as density, SSP, and RMS boundary roughness. Thus, in some cases it is possible that energy initially leaked from the layer in which transmission is occurring may reflect or refract back into that layer.

For the SSP and boundary conditions assumed in this thesis, the transmission loss values calculated by Bellhop are in close agreement to the greatly simplified transmission loss formula presented in this chapter. This suggests that over the short transmission paths investigated, bottom bounce losses were insignificant.

### 3. Noise Level

Noise at the receiver degrades its ability to process the arriving signal. When referring to noise, we specifically consider ambient noise resulting from a variety of sources such as biologic activity, seismic events, shipping, hydrodynamic noise, thermal noise, and surface noise resulting from surface winds and weather. During World War II, Wenz [20] developed a set of curves based on empirical data to quantify these various sources and the noise levels they could be expected to produce. There have since been many efforts to characterize noise in a variety of environments. Following from (2.9), the noise level may be expressed as [10]:

$$NL = NSL + 10 \log B \text{ dB re } 1 \mu\text{Pa}^2 \quad (2.25)$$

where NSL is the noise spectrum level, or the acoustic intensity measured over a spectral bandwidth of one hertz, given by [10]:

$$NSL = 10 \log \left( \frac{2S_{p_n}(f, \mathbf{r}_1)}{\mu\text{Pa}^2/\text{Hz}} \right) \text{ dB re } 1 \mu\text{Pa}^2/\text{Hz} \quad (2.26)$$

Since there are many distinct sources of noise in the ocean, the total NSL at a receiver located at  $\mathbf{r}_1$  is the power sum of the source levels of each contributing noise source. The total NSL may be expressed as:

$$NSL = 10 \log \left( \sum_i 10^{NSL_i/10} \right) \text{ dB re } 1 \mu\text{Pa}^2/\text{Hz} \quad (2.27)$$

Coates [10] developed a formula from empirical data that accounts for turbulence, shipping, surface agitation and thermal noise. Figure 8 shows Coates' values for (2.27) with a wind speed of 5 m/s and low shipping density. For the Seastar operating band of 35 to 55 kHz, according to [10], it is clear that the primary source of noise is surface noise (wind and wave noise).

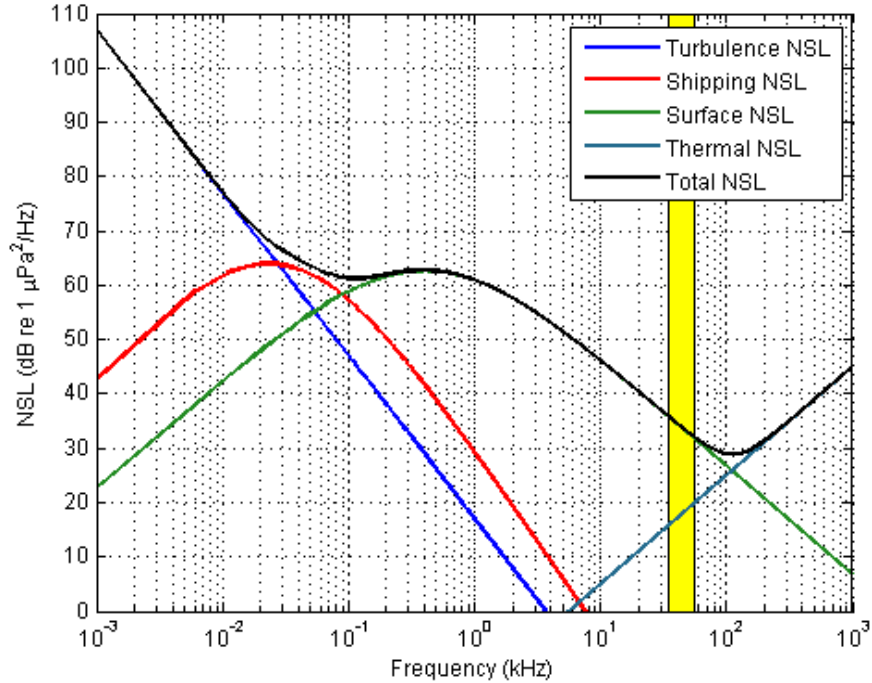


Figure 8. Noise spectrum level (NSL) for deep water as formulated by Coates [10]. A wind speed of 5 m/s and light shipping density are assumed.

It must be noted that Coates' empirical formula is based on data taken in deep water, while Seastar operates in shallow water. Coates also does not consider biologic noise like snapping shrimp, whose noise signatures are high amplitude and broadband, and can be found in many shallow-water environments [21]. Thus, using Coates' formula to represent the noise level across the frequency spectrum is useful only to the extent that it illustrates the sources of noise and relative spectra. To characterize an actual operating environment, it is preferable to have noise measurements from that environment, or others like it, to properly account for localized shipping density, biologic activity, weather patterns, and hydrodynamic turbulence.

The various sources of noise are known to exhibit certain statistical qualities [10]. Noise from surface agitation tends to vary slowly compared to other noise sources, since the surface retains inertia from the wind, and takes time to fully develop and dissipate. Shipping noise in a shallow environment varies relatively quickly, and tends to be composed of narrowband frequencies from engine and machinery noise. In coastal locations, breaking surf can contribute 10 dB more noise than deep water levels. Some biologics, such as whales and dolphins, produce calls that are quickly varying and narrowband in nature, while others, such as beds of snapping shrimp and fish choruses, produce slowly varying, broadband noise. Of importance to Seastar is the fact that shallow-water ambient noise varies more widely and more rapidly than deep-water ambient noise. This is particularly true near ports and shipping lanes, typical of environments where Seastar could operate.

#### **4. Transmission Frequency**

Transmission loss and noise both contribute to the degradation of underwater acoustic communications. By combining both of these quantities as expressed in (2.6), we are able to identify particular frequencies at which the highest  $\text{SNR}_a$  may be expected, thereby enabling us to determine a theoretical optimal operating band for the Seastar network [4]. Figure 9 shows  $\text{TL} + \text{NL}$  as a function of range and frequency in a channel having a temperature of 13°C, pH of 8.0, depth of 100 m, and salinity of 35 ppt, and where a surface wind speed is 5 m/s in an area with low shipping density. The solid black box signifies the ranges and frequency band in which Seastar is designed to operate.



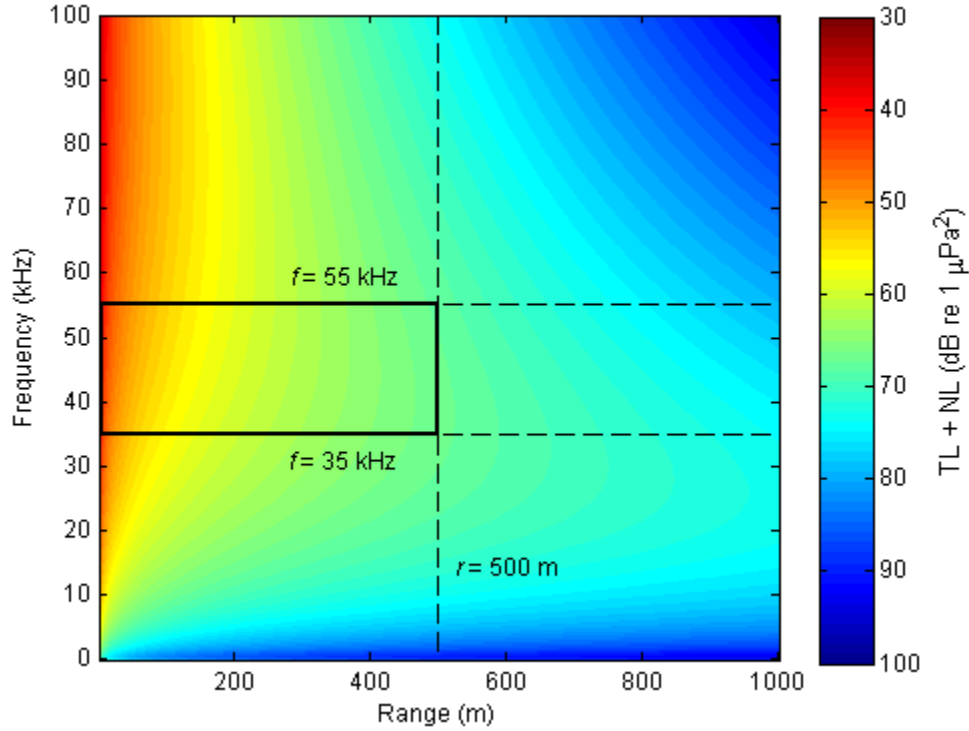


Figure 9. Transmission loss and noise level (from Coates) as a function of frequency and range.

Figure 10 shows TL + NL as a function of frequency at a range of 500 m for four wind speeds. As wind speed increases, noise from surface agitation rapidly increases across the Seastar operating band, which is denoted by the two dashed lines at 35 and 55 kHz. For the Seastar network, wind can be expected to play a significant role in communications performance, as the noise varies by decades of decibels for a change in wind speed of 15 m/s.

As discussed in the previous section, the NSL given by Coates' empirical formula are not necessarily representative of the shallow environment in which Seastar is designed to operate. We may nevertheless conclude that wind and sea state play a significant role in the performance of Seastar communications, and may indeed be the limiting factor for channel performance.

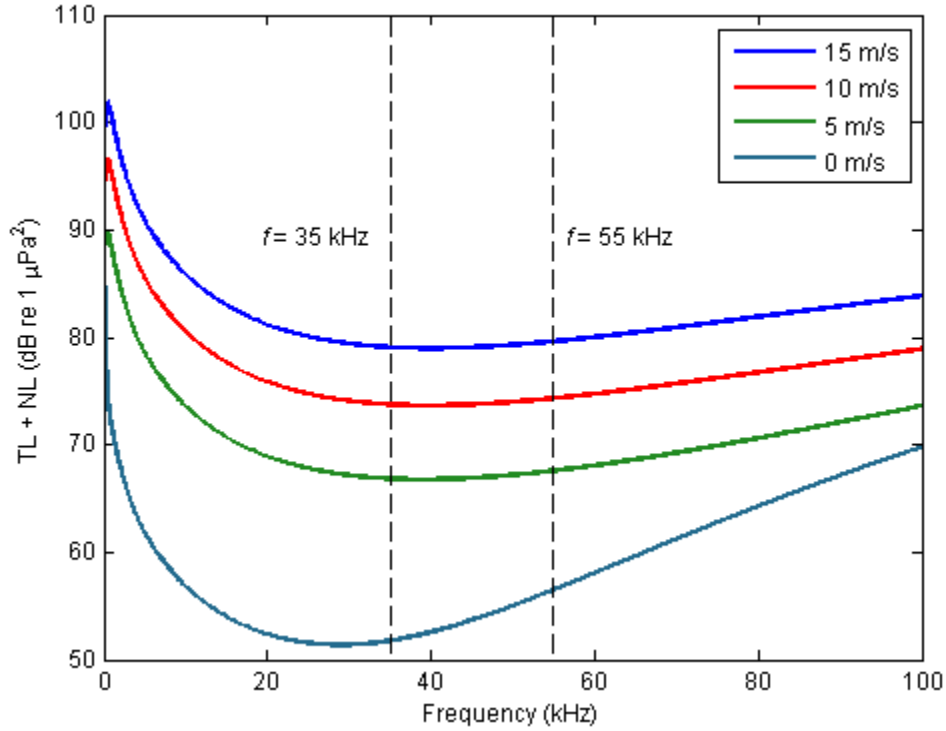


Figure 10. Transmission loss plus noise level (from Coates) as a function of frequency at a range of 500 m for four wind speeds.

#### D. THE FADING CHANNEL

The shallow, short-range, high-frequency underwater communication channel exhibits fading induced by multipath propagation. Multipath-induced fading occurs because of the presence of two reflecting boundaries: the surface and the bottom. When a ray interacts with one of these boundaries, the signal may encounter a shift in phase, frequency and amplitude. Each ray traverses a unique path, as illustrated by Figure 11, leading to unique travel times and boundary interactions for each ray. Thus, in a multipath-induced fading channel, a receiver hears multiple versions of the signal, each arriving at a different time, and having different phase, frequency, and amplitude than the original transmitted signal. The statistical characteristics of these multipath arrivals are directly dependent on the statistical characteristics of the boundaries with which the rays interact.

Further characterization of the fading channel can be made by determining whether the channel is flat or frequency-selective across the bandwidth of the signal, and if it is slow fading or fast fading [22]. For flat fading, the bandwidth of the signal is smaller than the coherence bandwidth of the channel, and the signal is attenuated evenly across all frequencies. For frequency-selective fading, the bandwidth of the signal is greater than the coherence bandwidth of the channel, and the signal experiences non-uniform attenuation at different frequencies. Frequency-selective fading is commonly modeled using Rayleigh-, Rician-, and Nakagami-distributed attenuation [22]. From our previous discussion regarding noise and transmission loss, we know that the underwater acoustic communication channel is most definitely frequency-selective. Thus, signals used in the Seastar network can be expected to experience frequency-selective fading.

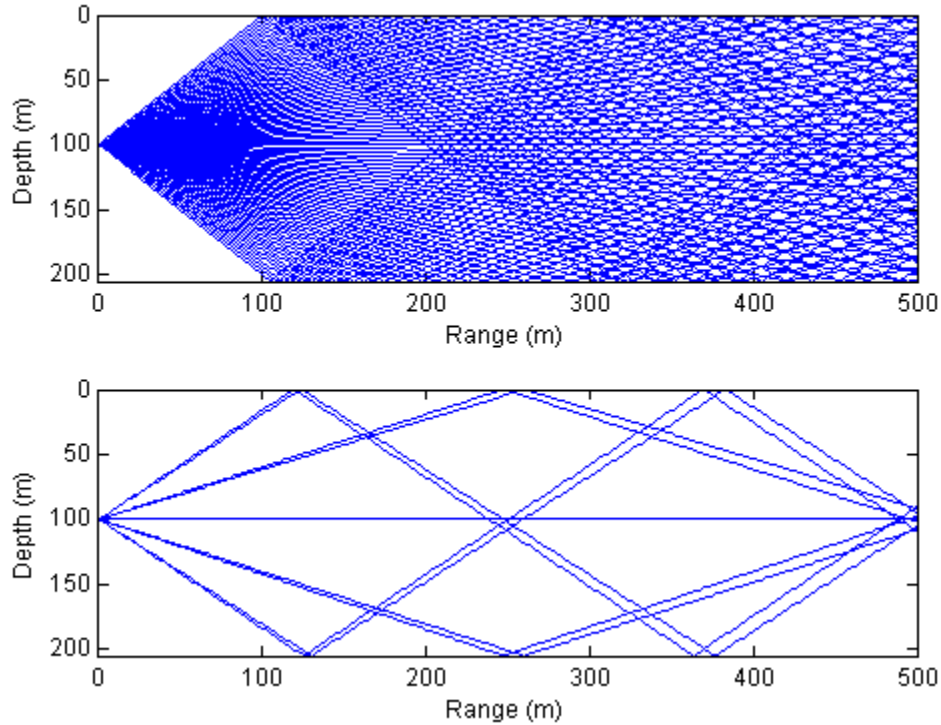


Figure 11. The upper plot is a Bellhop ray trace for a fan of 91 Gaussian beams in an isospeed sound channel. The lower plot displays the eigenrays, or those rays that intercept a receiver at range  $r = 500$  m.

## 1. Multipath Spread

The time spread of a signal refers to the spreading out, in time, of the transmitted signal as it propagates to the receiver. A signal can experience time spreading as a result of a variety of phenomena, including multipath propagation. As the multipath rays arrive at the receiver, the resulting received signal, when compared to the transmitted version of the signal, may appear to have spread in time. Thus, it may be said that multipath propagation lengthens the channel's impulse response, which in turn causes the received signal to spread in time. The time interval over which these multipath signals arrive at the receiver is called the multipath spread of the channel, and is denoted by  $T_m$  [22]. The multipath spread of the channel can be inversely represented in frequency by the coherence bandwidth of the channel, given by [22]:

$$(\Delta f)_c \approx \frac{1}{T_m} \quad (2.28)$$

If the bandwidth of the transmitted signal is greater than (2.28), the channel is frequency-selective. If the bandwidth of the transmitted signal is less than (2.28), the channel is frequency-nonselective.

## 2. Doppler Spread

The range of frequencies over which the Doppler power spectrum of the channel is nonzero is called the Doppler spread of the channel, and is denoted by  $B_d$  [22]. Doppler spread can be inversely represented in time by the coherence time of the channel, given by [22]:

$$(\Delta t)_c \approx \frac{1}{B_d} \quad (2.29)$$

Longer values for (2.29), and equivalently, smaller values for  $B_d$ , correspond to a slow-fading channel, while smaller values for (2.29) correspond to a fast-fading channel.

Doppler spread occurs as a result of Doppler shifts caused by motion at the source, receiver, and channel boundaries. Mobile nodes exhibit a Doppler shift proportional to their relative velocity, while currents and tides can also force moored nodes to move, introducing slight Doppler shifts. The boundaries can introduce Doppler

shifts when rays interact with gravity waves; this is particularly evident at the surface, but can also occur in stratified water in which internal waves may be propagating.

Let us explicitly examine the effect of velocity on frequency using the receiver as a reference. Assuming the speed of the current in the channel is zero, the frequency observed at the receiver is given by [23]:

$$f' = \left( \frac{c + v_r}{c + v_s} \right) f \quad (2.30)$$

where  $f'$  is the observed frequency at the receiver,  $c$  is the speed of sound,  $v_s$  is the radial component of the velocity of the source,  $v_r$  is the radial component of the velocity of the receiver, and  $f$  is the transmitted frequency at the source. Consider, for example, the case of a mobile source and a stationary receiver where  $v_r$  is zero. Equation (2.30) then simplifies to:

$$f' = \left( \frac{c}{c + v_s} \right) f \quad (2.31)$$

where  $v_s$  is positive if the source is moving away from the receiver, and negative if the source is moving towards the receiver. The frequency observed at the receiver is lower than the transmitted frequency if  $v_s$  is positive, and higher if  $v_s$  is negative.

In multipath propagation, a Doppler shift can occur every time a ray interacts with a boundary. Thus, the frequency observed at the receiver is a combination of all the various frequency shifts the signal has encountered through its multipath propagation. These shifts contribute to the formation of the multipath-induced fading channel. Because the Doppler shifts are velocity dependent, the more perturbed the boundaries are, for instance due to a large sea state, the greater the Doppler shifts will be. For stationary boundary conditions, reflections do not introduce Doppler shifts.

Doppler spread is the accumulation of the total effects that motion at the source, receiver, and channel boundaries have on the frequency observed at the receiver. The spread refers to the tendency of a transmitted signal's bandwidth  $B$  to spread out in the frequency domain as it propagates through the fading channel. The bandwidth of the

signal observed at the receiver may then be  $B + \Delta B$ , where  $\Delta B$  is the additional bandwidth the received signal occupies as a result of propagating through a fading channel.

### 3. Intersymbol Interference

Intersymbol interference (ISI) is a form of distortion of a signal in which one symbol interferes with subsequent symbols. This is an undesirable phenomenon, as the previous symbols have a similar effect as noise, thus making communications less reliable. ISI is usually caused by multipath spread of the inherent nonlinear frequency response of a channel, causing successive symbols to “blur” together. The presence of ISI in the system introduces errors in the decision device at the receiver output.

In Seastar, ISI can be pronounced due to the large multipath spread of the short-range channel. Figure 12 shows a long-range source-receiver configuration. Shown are two eigenrays, the direct path and the surface-reflected path. The time difference of arrival between the two rays is depicted pictorially as pulse trains, and we see that, compared to the pulse duration  $T$ , this multipath spread  $T_m$  is relatively small, corresponding to relatively small overlap between symbols, and therefore low ISI. In Figure 13, a short-range source-receiver configuration is shown. In this case,  $T_m$  is large compared to the pulse duration  $T$ , corresponding to relatively large overlap between symbols, and therefore more ISI. If  $T$  is shortened, the overlap becomes even greater. These relationships are examined further in Chapter V.

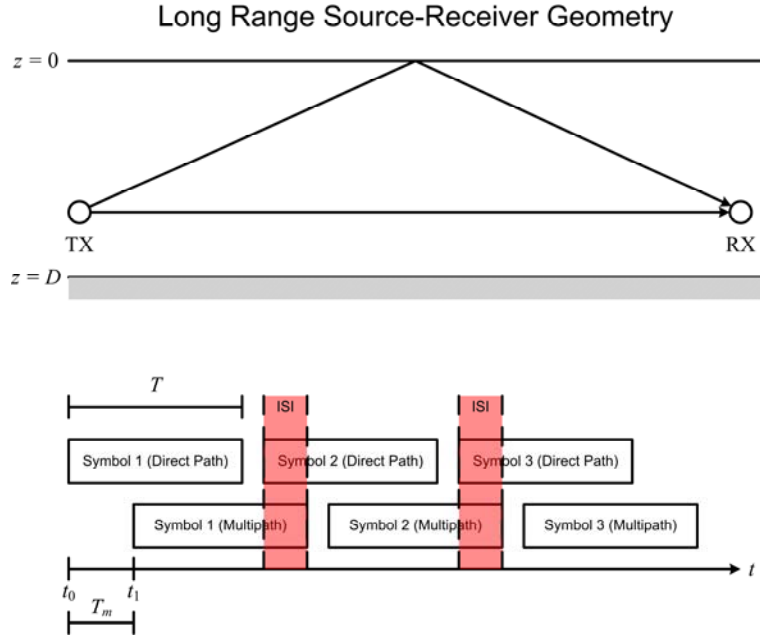


Figure 12. Direct-path and surface-reflected path pulse trains for a long-range source-receiver geometry.

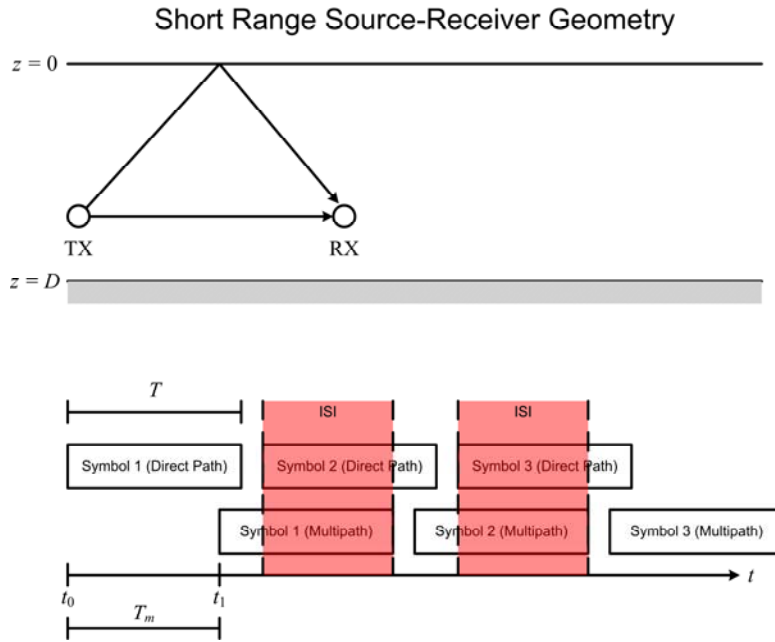


Figure 13. Direct-path and surface-reflected path pulse trains for a short-range source-receiver geometry.

THIS PAGE INTENTIONALLY LEFT BLANK



### III. MULTI-CHANNEL M-ARY FREQUENCY-SHIFT KEYING

Both Seastar and Seaweb modems use a modulation scheme commonly referred to as multi-channel MFSK. However, this title is not entirely descriptive of how the modulation scheme actually works [3, 24]. We now present a mathematical representation of the multi-channel MFSK modulation scheme.

#### A. MODULATION

Before representing multi-channel MFSK mathematically, it is useful and necessary to define pure MFSK. In MFSK [25-27],  $M$  frequencies, each offset from a center frequency, are used to transmit  $M$  unique channel symbols; each symbol therefore corresponds to its own unique frequency.

Traditionally, the total number of channel symbols, and therefore frequencies, is determined by how many bits per symbol are used. However, in Seastar, due to signaling techniques applied before modulation, such as convolution coding and interleaving, it is more accurate to replace our use of the word “bits” with “encoded symbols.” This releases us from confusing bits that are truly fed into the communication system before coding and interleaving with bits that form channel symbols within the demodulator. The number of possible channel symbols, and therefore frequencies, is thus determined by how many encoded symbols are used for each channel symbol.

In Seastar, there are two encoded symbols per channel symbol used. The number of unique channel symbols  $M$  is given by  $M = 2^{n_b}$ , where  $n_b$  is the number of encoded symbols per channel symbol. Seastar uses an  $M = 4$  alphabet, so that there are four unique channel symbols, transmitted with four unique frequencies. This configuration is referred to as 1-in-4 FSK, or 4-ary FSK, because only one of a possible four unique transmission frequencies is actively transmitting at any instant [3, 24]. In the time domain, the MFSK waveform may be represented as a pulse train, and is given by [4]:

$$x(t) = \sum_{n=1}^N x_n(t - t_n), \quad 0 \leq t \leq T_d \quad (3.1)$$

where the  $n^{\text{th}}$  pulse, corresponding to one of the  $M$  symbols, is:

$$x_n(t) = A \cos(2\pi[f_c + \Delta f_n]t + \varepsilon_n) \text{rect}\left(\frac{t - 0.5T}{T}\right) \quad (3.2)$$

where

$N$ : Number of pulses (channel symbols) transmitted in the time interval  
 $0 \leq t \leq T_d$

$t_n$ : Time instant when the  $n^{\text{th}}$  pulse begins (seconds)

$T_d$ : Duration of the transmitted pulse train (seconds)

$A$ : Amplitude

$f_c$ : Carrier frequency (hertz)

$\Delta f_n$ : Frequency offset of the  $n^{\text{th}}$  pulse (hertz)

$\varepsilon_n$ : Introduced phase shift of the  $n^{\text{th}}$  pulse (radians)

$T$ : Pulse duration, or symbol duration (seconds)

$$\text{rect}\left(\frac{t - 0.5T}{T}\right) = \begin{cases} 1, & 0 \leq t \leq T \\ 0, & \text{otherwise} \end{cases} \quad (3.3)$$

The total signal duration can subsequently be expressed as  $NT$  seconds. The phase shift  $\varepsilon_n$  is included in (3.2) and subsequent representations because unintentional phase shifts are often introduced during communication.

The frequency offset  $\Delta f_n$  is given by:

$$\Delta f_n = \frac{k_n}{2T} \quad (3.4)$$

where  $k_n$  is an integer that determines the frequency offset of the  $n^{\text{th}}$  pulse. In order to accurately represent the Seastar modulation scheme, it is necessary that we adopt  $k_n \in \{\pm 1, \pm 3, \dots, \pm(M-1)\}$ . This particular set of  $k_n$  ensures that the spectral spacing between each unique frequency is equal to  $1/T$  and that the individual pulses are orthogonal, even with phase shift  $\varepsilon_n$ . The condition of orthogonality can be illustrated with the following relationship [4]:

$$\langle x_m(t), x_n(t) \rangle = \int_{-\infty}^{\infty} x_m(t) x_n^*(t) dt = E_{x_m} \delta_{m,n}, \quad m, n = 1, 2, \dots, M \quad (3.5)$$

where  $\delta_{m,n}$  is the Kronecker delta and  $E_{x_m}$  is the energy contained in symbol  $m$ , given by:

$$E_{x_m} = \langle x_m(t), x_m(t) \rangle = \int_{-\infty}^{\infty} |x_m(t)|^2 dt = \frac{1}{2} A^2 T, \quad m = 1, 2, \dots, M \quad (3.6)$$

From the MFSK pulse train representation in the time domain, we obtain the Fourier transform of (3.1):

$$\begin{aligned} X(f) &= \frac{AT}{2} e^{j\pi(f+f_c)T} \sum_{n=1}^N \text{sinc}\left\{[f - (f_c + \Delta f_n)]T\right\} e^{j\pi\Delta f_n T} e^{-j2\pi f_n T} e^{j\epsilon_n} + \\ &\quad \frac{AT}{2} e^{j\pi(f-f_c)T} \sum_{n=1}^N \text{sinc}\left\{[f + (f_c + \Delta f_n)]T\right\} e^{-j\pi\Delta f_n T} e^{-j2\pi f_n T} e^{-j\epsilon_n} \end{aligned} \quad (3.7)$$

The MFSK waveform in the frequency domain is thus a summation of sinc functions whose peaks occur along the positive frequency axis at  $f = f_c + \Delta f_n$ , and whose zero crossings occur every  $1/T$  from  $f$  [4]. As illustrated in Figure 14, the occurrence of a particular sinc function's peak at the zero crossings of the other sinc functions, along with the exact overlapping of the functions' zero crossings, is consistent with the condition of orthogonality.

A generally accepted approach to estimating a signal's bandwidth is to extend the bandwidth out to the limit where the magnitude of the spectrum is an order of magnitude lower than its maximum value. For instance, the unit-amplitude sinc function's bandwidth might be defined as the frequency interval between where  $|\text{sinc}(fT)| \geq 0.1$  for  $f > 3/T$ , or where the power is 20 dB down from the maximum power. Thus, a pulse's bandwidth—which is altogether a different quantity from the frequency offset—might be defined as:

$$BW_m = \frac{3}{T} - \left(-\frac{3}{T}\right) = \frac{6}{T} \quad (3.8)$$

Due to the specified condition of orthogonality, and the fact that most of the energy contained in the signal is located between the first zero crossings,  $1/T$  serves as a

useful frequency offset in modulation and frequency bin width in demodulation, but is not necessarily an accurate representation of the signal's true bandwidth.

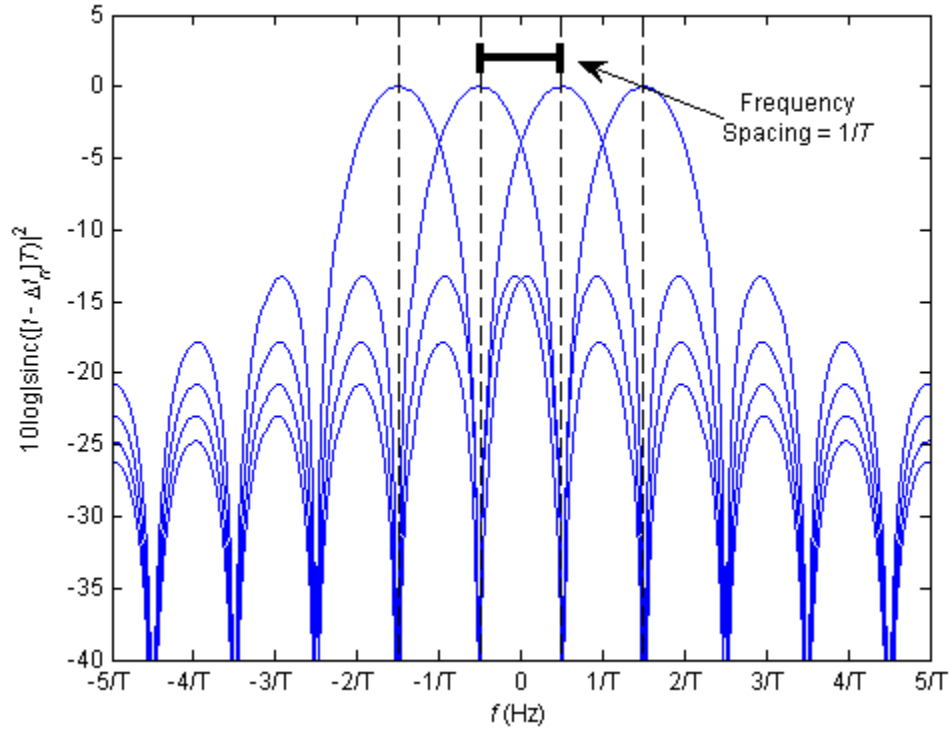


Figure 14. Normalized power spectra for four orthogonally spaced sinc functions. The spacing between any two functions' peaks is  $1/T$ , so that peaks are centered at the other functions' zero crossings.

Now that pure MFSK has been discussed, it is possible to mathematically define the multi-channel MFSK waveform used aboard the Seastar modems. By multi-channel MFSK, we mean to transmit several MFSK pulse trains, or channels, by using frequency-division multiplexing (FDM). Signals that are transmitted using FDM are fed into a modulator that simply sums the signals [28]. Each signal has its own, unique carrier frequency known as a subcarrier frequency. In FDM, the input signals may be modulated using any variety of schemes, including amplitude modulation, phase modulation, frequency modulation, and any of the digital modulation techniques that exist. For Seaweb and Seastar, MFSK has been chosen because it has proven to be a robust and reliable waveform in underwater data transmission [5].

Multi-channel MFSK allows us to transmit  $I$  channels of MFSK pulse trains simultaneously. The scheme thus permits data to be transmitted in parallel, allowing for data rates that are higher than a single MFSK pulse train by a factor of  $I$ . In the case of Seastar,  $I = 32$  channels (32 pulse trains), and the entire waveform is spread across 5120 Hz of bandwidth [3, 24]. At any particular time during transmission, there are subsequently 32 channels of 4-ary FSK pulse trains, where each subpulse of a particular pulse train has one of four possible frequencies corresponding to one of the four unique channel symbols.

Combining the mathematical representations of MFSK and FDM, we develop a general and analytical representation for multi-channel MFSK:

$$x(t) = \sum_{i=1}^I \sum_{n=1}^N x_{n,i}(t - t_n), \quad 0 \leq t \leq T_d \quad (3.9)$$

where the  $n^{\text{th}}$  pulse of the  $i^{\text{th}}$  channel is given by:

$$x_{n,i}(t) = A_i \cos\left(2\pi \left[f_{c,i} + \Delta f_{n,i}\right]t + \varepsilon_{n,i}\right) \text{rect}\left(\frac{t - 0.5T}{T}\right) \quad (3.10)$$

where

- $I$ : Number of “channels,” or MFSK pulse trains
- $N$ : Number of pulses (channel symbols) transmitted in the time interval  $0 \leq t \leq T_d$
- $t_n$ : Time instant when the  $n^{\text{th}}$  pulse begins (seconds)
- $T_d$ : Duration of the transmitted pulse train (seconds)
- $A_i$ : Amplitude of the  $i^{\text{th}}$  channel
- $f_{c,i}$ : Subcarrier frequency of the  $i^{\text{th}}$  channel (hertz)
- $\Delta f_{n,i}$ : Frequency offset of the  $n^{\text{th}}$  pulse of the  $i^{\text{th}}$  channel (hertz)
- $\varepsilon_{n,i}$ : Introduced phase shift of the  $n^{\text{th}}$  pulse of the  $i^{\text{th}}$  channel (radians)
- $T$ : Pulse duration, or symbol duration (seconds)

$$\text{rect}\left(\frac{t-0.5T}{T}\right) = \begin{cases} 1, & 0 \leq t \leq T \\ 0, & \text{otherwise} \end{cases} \quad (3.3)$$

The frequency offset  $\Delta f_{n,i}$  is given by:

$$\Delta f_{n,i} = \frac{k_{n,i}}{2T} \quad (3.11)$$

where  $k_{n,i} \in \{\pm 1, \pm 3, \dots, \pm(M-1)\}$ . The subcarrier frequency may be expressed as:

$$f_{c,i} = f_c + f_i \quad (3.12)$$

where

$$f_i = \frac{a_i M}{2T} \quad (3.13)$$

where  $f_c$  is the carrier frequency of the entire multi-channel MFSK signal,  $f_i$  determines the frequency spacing of the  $i^{\text{th}}$  channel, and  $a_i \in \{\pm 1, \pm 3, \dots, \pm(I-1)\}$ .

We obtain the frequency spectrum of the multi-channel MFSK signal by taking the Fourier transform of (3.9):

$$\begin{aligned} X(f) = & \frac{AT}{2} \sum_{i=1}^I e^{j\pi(f+f_{c,i})T} \sum_{n=1}^N \text{sinc}\left\{\left[f - (f_{c,i} + \Delta f_{n,i})\right]T\right\} e^{j\pi\Delta f_{n,i}T} e^{-j2\pi f n T} e^{j\epsilon_{n,i}} + \\ & \frac{AT}{2} \sum_{i=1}^I e^{j\pi(f-f_{c,i})T} \sum_{n=1}^N \text{sinc}\left\{\left[f + (f_{c,i} + \Delta f_{n,i})\right]T\right\} e^{-j\pi\Delta f_{n,i}T} e^{-j2\pi f n T} e^{-j\epsilon_{n,i}} \end{aligned} \quad (3.14)$$

The frequency spectrum of (3.9) given by (3.14) is pictured in Figure 15, where the power spectral density is given by:

$$S(f) = X(f) X^*(f) = |X(f)|^2 \quad (3.15)$$

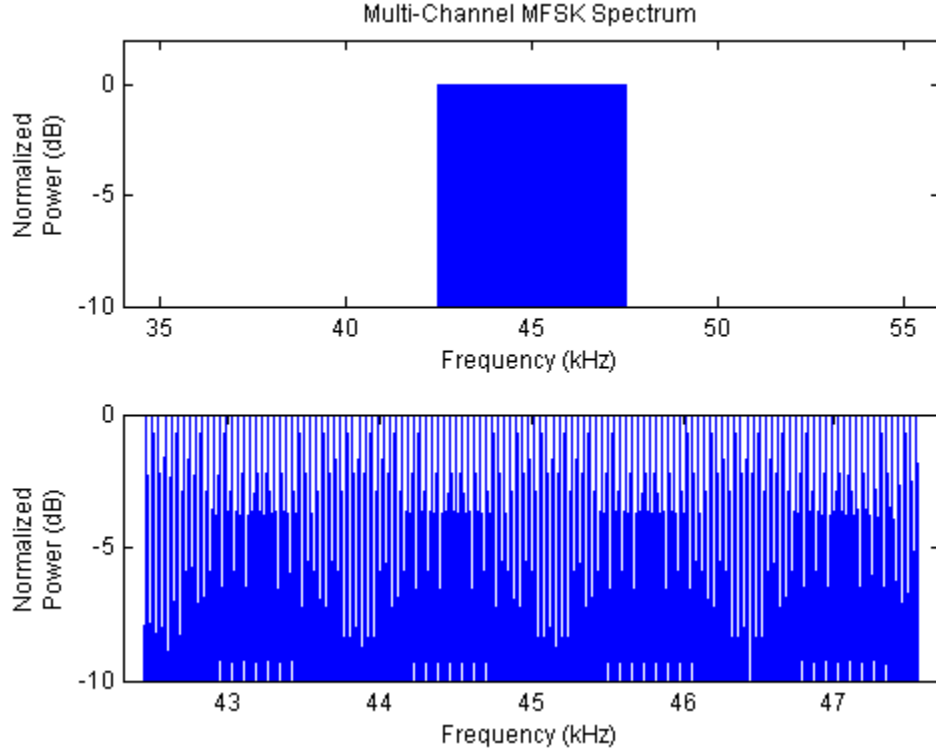


Figure 15. Frequency spectrum of the multi-channel MFSK waveform centered at 45 kHz,  $T = 25$  ms. Shown are 32 channels (pulse trains) of 4-ary FSK.

The construction of the multi-channel MFSK signal can be accomplished practically by heterodyning the MFSK pulse train given by (3.1) with a time-harmonic signal of frequency  $f_i$ . This form of modulation is shown in Figure 16, where  $x_i(t)$  has a carrier frequency of  $f_c$ , and the resulting subcarrier frequencies of  $x(t)$  are given by (3.12).

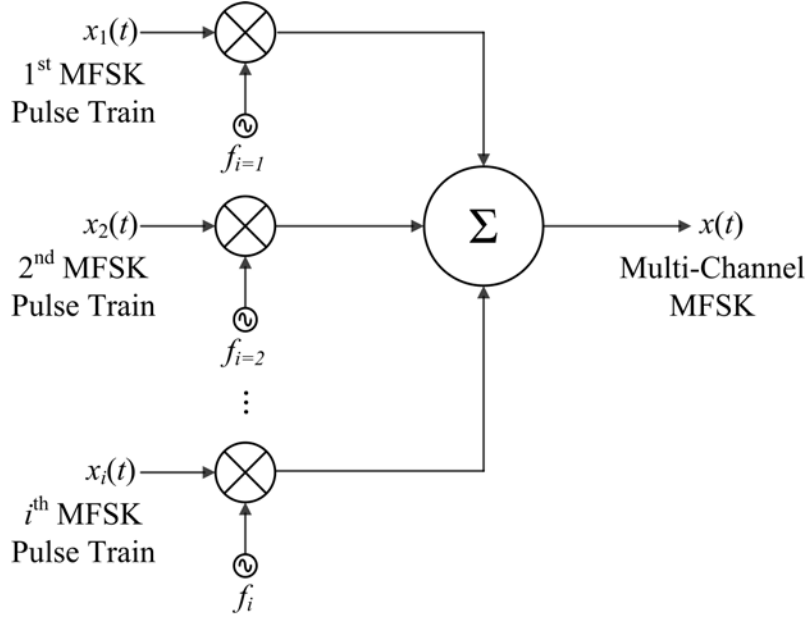


Figure 16. Frequency-division multiplexing of the MFSK channels (pulse trains) produces the multi-channel MFSK waveform  $x(t)$ .

In multi-channel MFSK, each subcarrier frequency is orthogonally spaced, which makes it similar to orthogonal frequency-division multiplexing (OFDM). However, though the subcarriers are orthogonal to each other, we restrict ourselves from calling it OFDM, since OFDM does not encode symbols using different frequencies. In multi-channel MFSK, demodulation does not require phase information to be preserved, since symbols are represented in the frequency domain only. With OFDM, symbols can be represented by amplitude, phase, or both, making the modulation scheme vulnerable to phase shifts and amplitude attenuation. Furthermore, the encoding of symbols using phase introduces an additional layer of demodulation and processing that acts as a sink in the very limited power supply of a remote acoustic communication node.

Figure 17 shows a spectrogram of the multi-channel MSFK waveform used in Seaweb. The signal has a pulse duration of 25 ms, and a bandwidth of 5120 Hz. In this particular figure, each pulse is repeated once. We can see that at any one instant, only 32 tones are transmitted. When the next pulse arrives, a different set of 32 tones are transmitted.



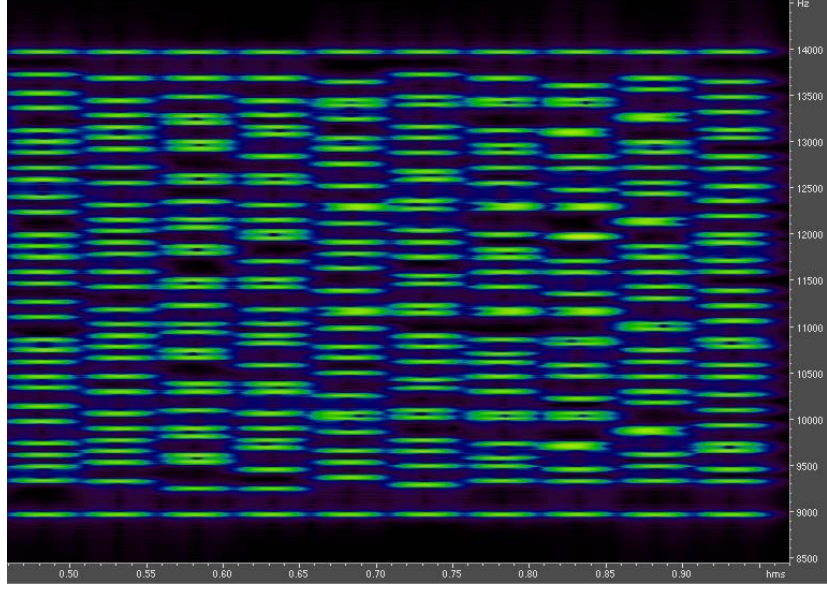


Figure 17. Spectrogram of the multi-channel MFSK signal used in Seaweb. The abscissa is time, and the ordinate is frequency.

## B. IMPLEMENTATION

### 1. Bandwidth Scaling

Bandwidth scaling is based on the time-frequency scaling property of Fourier analysis, and is currently in use aboard Seastar modems. Implementing bandwidth scaling simply requires introducing a scaling factor  $s$  into (3.1). The resulting bandwidth-scaled signal is:

$$x(st) = \sum_{i=1}^I \sum_{n=1}^N x_{n,i}(st - t_n), \quad 0 \leq t \leq \frac{T_d}{s} \quad (3.16)$$

where the  $n^{\text{th}}$  pulse of the  $i^{\text{th}}$  channel is given by:

$$x_{n,i}(st) = A_i \cos\left(2\pi \left[f_{c,i} + \Delta f_{n,i}\right] st + \varepsilon_{n,i}\right) \text{rect}\left(\frac{st - 0.5T}{T}\right) \quad (3.17)$$

where

$$\text{rect}\left(\frac{st - 0.5T}{T}\right) = \begin{cases} 1, & 0 \leq t \leq \frac{T}{s} \\ 0, & \text{otherwise} \end{cases} \quad (3.18)$$

$$f_i = \frac{a_i M}{2(T/s)} = \frac{sa_i M}{2T} \quad (3.19)$$

$$\Delta f_{n,i} = \frac{k_{n,i}}{2(T/s)} = \frac{sk_{n,i}}{2T} \quad (3.20)$$

From (3.16), we observe that in addition to time scaling (3.17) by a factor of  $s$ , we can include  $t_n$  in the argument for  $x_{n,i}(st)$ , which gives:

$$x_{n,i}(st - t_n) = A_i \cos\left(2\pi\left[f_{c,i} + \Delta f_{n,i}\right][st - t_n] + \varepsilon_{n,i}\right) \text{rect}\left(\frac{st - t_n - 0.5T}{T}\right) \quad (3.21)$$

We obtain the frequency spectrum of the bandwidth-scaled multi-channel MFSK signal by taking the Fourier transform of (3.16):

$$\begin{aligned} X(f) = & \frac{AT}{2|s|} \sum_{i=1}^I e^{j\pi\left(\frac{f}{s} + f_{c,i}\right)T} \sum_{n=1}^N \text{sinc}\left\{\left[\frac{f}{s} - (f_{c,i} + \Delta f_{n,i})\right]T\right\} e^{j\pi\Delta f_{n,i}T} e^{-j2\pi\frac{f}{s}nT} e^{j\varepsilon_{n,i}} + \\ & \frac{AT}{2|s|} \sum_{i=1}^I e^{j\pi\left(\frac{f}{s} - f_{c,i}\right)T} \sum_{n=1}^N \text{sinc}\left\{\left[\frac{f}{s} + (f_{c,i} + \Delta f_{n,i})\right]T\right\} e^{-j\pi\Delta f_{n,i}T} e^{-j2\pi\frac{f}{s}nT} e^{-j\varepsilon_{n,i}} \end{aligned} \quad (3.22)$$

The frequency spectrum of (3.16) given by (3.22) is pictured in Figure 18, where the power spectral density is given by (3.15).

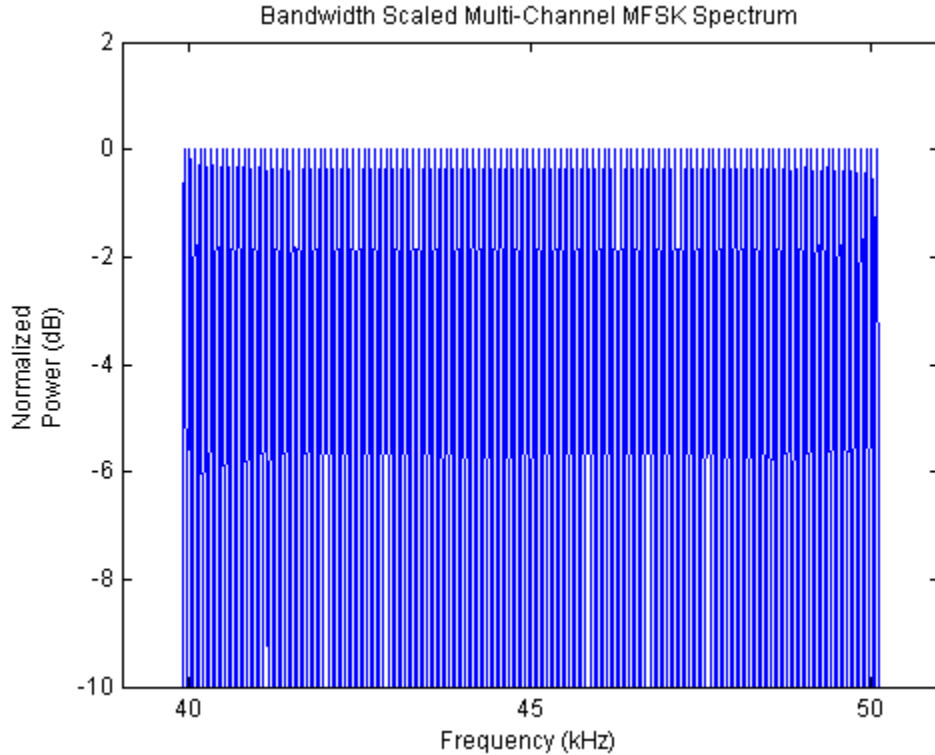


Figure 18. Frequency spectrum of the bandwidth-scaled multi-channel MFSK waveform centered at 45 kHz,  $T = 12.5$  ms. Shown are 32 channels of 4-ary FSK.

In implementing multi-channel MFSK by bandwidth scaling,  $s$  is chosen to be greater than unity, so that the signal becomes shortened in the time domain and stretched in the frequency domain.

Provided that sufficient bandwidth is available, bandwidth scaling is a useful and practical way to increase the data rate. With  $s > 1$ , bandwidth scaling is further advantageous in that it becomes less vulnerable to Doppler spread, since the bandwidth of the individual subpulses and the frequency bins are stretched by a factor of  $s$ . The values of the Doppler shifts experienced by a particular path consequently become smaller relative to  $1/T$ . However, for  $s > 1$ , the signal is more susceptible to ISI due to the shortening of the pulse duration  $T$ . In the short-range, high-frequency underwater acoustic communication channel, where a signal is continuously transmitted, it is shown in Chapter V that a shortened pulse duration  $T$  increases the time difference of arrival between the direct path and the next multipath arrivals of a signal, and ultimately increases the multipath spread of the received signal.

## 2. Frequency Multiplexing

In this thesis, the term frequency multiplexing as it pertains to multi-channel MFSK refers to the transmission of the original 5 kHz format across additional bands. This modulation technique adds an additional tier of the FDM pictured in Figure 16. The frequency-multiplexed multi-channel MFSK signal may be represented in the time domain by:

$$x(t) = \sum_{j=1}^J \sum_{i=1}^I \sum_{n=1}^N x_{n,i,j}(t - t_n), \quad 0 \leq t \leq T_d \quad (3.23)$$

where the  $n^{\text{th}}$  pulse of the  $i^{\text{th}}$  channel in the  $j^{\text{th}}$  band is given by:

$$x_{n,i,j}(t) = A_{i,j} \cos\left(2\pi\left[f_{c,i,j} + \Delta f_{n,i,j}\right]t + \varepsilon_{n,i,j}\right) \text{rect}\left(\frac{t - 0.5T}{T}\right) \quad (3.24)$$

where

$J$ : Number of bands of multi-channel MFSK

$I$ : Number of “channels,” or MFSK pulse trains

- $N$ : Number of pulses (channel symbols) transmitted in the time interval  $0 \leq t \leq T_d$
- $t_n$ : Time instant when the  $n^{\text{th}}$  pulse begins (seconds)
- $T_d$ : Duration of the transmitted signal (seconds)
- $A_{i,j}$ : Amplitude of the  $i^{\text{th}}$  channel in the  $j^{\text{th}}$  band
- $f_{c,i,j}$ : Subcarrier frequency of the  $i^{\text{th}}$  channel in the  $j^{\text{th}}$  band (hertz)
- $\Delta f_{n,i,j}$ : Frequency offset of the  $n^{\text{th}}$  pulse of the  $i^{\text{th}}$  channel in the  $j^{\text{th}}$  band (hertz)
- $\varepsilon_{n,i,j}$ : Introduced phase shift of the  $n^{\text{th}}$  pulse of the  $i^{\text{th}}$  channel in the  $j^{\text{th}}$  band (radians)
- $T$ : Pulse duration, or symbol duration (seconds)

$$\text{rect}\left(\frac{t - 0.5T}{T}\right) = \begin{cases} 1, & 0 \leq t \leq T \\ 0, & \text{otherwise} \end{cases} \quad (3.3)$$

The frequency offset  $\Delta f_{n,i,j}$  is given by:

$$\Delta f_{n,i,j} = \frac{k_{n,i,j}}{2T} \quad (3.25)$$

where  $k_{n,i,j} \in \{\pm 1, \pm 3, \dots, \pm(M-1)\}$ . The subcarrier frequency may be expressed as:

$$f_{c,i,j} = f_c + f_{i,j} \quad (3.26)$$

where

$$f_{i,j} = \frac{a_i M}{2T} + \frac{b_j I M}{2T} \quad (3.27)$$

where  $f_c$  is the carrier frequency of the entire frequency-multiplexed multi-channel MFSK signal,  $f_{i,j}$  determines the frequency spacing of the  $i^{\text{th}}$  channel in the  $j^{\text{th}}$  band,  $a_i \in \{\pm 1, \pm 3, \dots, \pm(I-1)\}$ , and  $b_j \in \{\pm 1, \pm 3, \dots, \pm(J-1)\}$ .

We obtain the frequency spectrum of the frequency-multiplexed multi-channel MFSK signal by taking the Fourier transform of (3.23):

$$\begin{aligned}
X(f) = & \frac{AT}{2} \sum_{j=1}^J \sum_{i=1}^I e^{j\pi(f+f_{c,i,j})T} \sum_{n=1}^N \text{sinc}\left\{\left[f - (f_{c,i,j} + \Delta f_{n,i,j})\right]T\right\} e^{j\pi\Delta f_{n,i,j}T} e^{-j2\pi fnT} e^{j\epsilon_{n,i,j}} + \\
& \frac{AT}{2} \sum_{j=1}^J \sum_{i=1}^I e^{j\pi(f-f_{c,i,j})T} \sum_{n=1}^N \text{sinc}\left\{\left[f + (f_{c,i,j} + \Delta f_{n,i,j})\right]T\right\} e^{-j\pi\Delta f_{n,i,j}T} e^{-j2\pi fnT} e^{-j\epsilon_{n,i,j}}
\end{aligned} \tag{3.28}$$

The frequency spectrum of (3.23) given by (3.28) is pictured in Figure 19, where the power spectral density is given by (3.15).

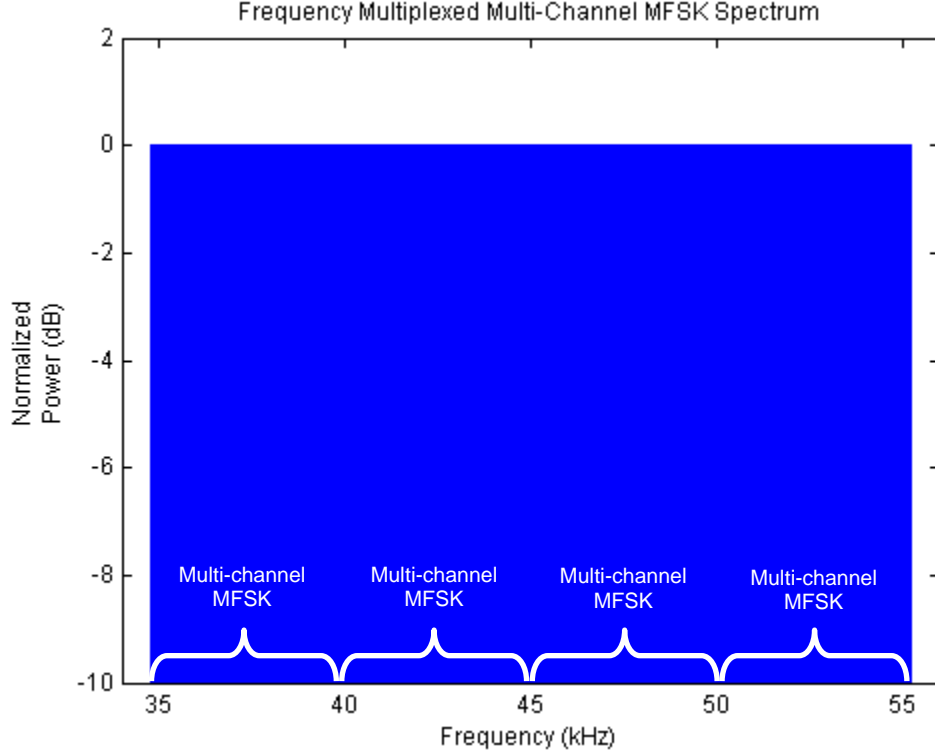


Figure 19. Frequency spectrum of the frequency-multiplexed multi-channel MFSK waveform centered at 45 kHz,  $T = 25$  ms. Shown are 4 bands of 32 channels of 4-ary FSK.

Frequency multiplexing allows for higher data rates to be achieved without shortening the pulse duration  $T$ . Maintaining a longer pulse duration protects against ISI in the short-range, high-frequency underwater communication channel, and makes the signal more immune to multipath spread. However, a significant drawback lies in the fact that there is less tolerance for Doppler spread compared to a bandwidth-scaled multi-channel MFSK signal, since the values of the Doppler shifts experienced by a particular path consequently become larger relative to  $1/T$ .

THIS PAGE INTENTIONALLY LEFT BLANK

## IV. DEMODULATION

Demodulation is accomplished by examining the frequency content of the multi-channel MFSK signal with the use of the discrete Fourier transform (DFT), computed by the FFT algorithm, over each pulse duration  $T$ . At the receiver, a band-pass filter can be applied across the known operating band of the signal, so that only frequencies at which we expect information are processed. The received signal is then basebanded through heterodyning, and the multi-channel MFSK spectrum is divided into frequency bins that are  $1/T$  Hz wide. With an appropriately sized FFT, each bin potentially contains one tonal. If there are 32 channels, or pulse trains, of 4-ary FSK being transmitted, as in the case of Seastar, then 32 of a possible 128 bins would contain energy from a subpulse. The 128 bins are subsequently divided into 32 groups of four, where each of the four bins corresponds to one of the unique channel symbols determined by the  $M = 4$  alphabet. Comparative decision logic is then applied such that the bin containing the greatest amount of energy determines what channel symbol is being received. This approach is implemented in the simulations presented in Chapter V, but for a single channel of 4-ary FSK instead of the entire multi-channel MFSK signal.

For the demodulation of the frequency-multiplexed implementation of multi-channel MFSK, a band-pass filter can be applied to isolate the  $J$  bands of multi-channel MFSK, and the same FFT demodulation process repeated for each of these bands.

A useful metric in analyzing the performance characteristics of a particular digital modulation scheme is the encoded SER. The encoded SER is determined by dividing the number of encoded symbol errors in the received signal by the total number of encoded symbols transmitted over the duration of the signal. Encoded symbol errors can result during the demodulation of a signal that is distorted by noise or interference. The encoded SER is used to measure modulation scheme performance in the simulations presented in Chapter V.

Similar to SER is the bit error rate (BER), which is the number of bits received in error divided by the total number of transmitted bits. For BER analysis, noise is quantified by the energy per encoded symbol to noise power spectral density ratio, given by:

$$E_b/N_0 \quad (4.4)$$

To achieve accurate values for both the SER and the BER, a large number of encoded symbols and bits must be transmitted through a noisy channel, often on the order of  $10^6$  or greater. The requirement for a large amount of symbols transmitted is especially pertinent for channels with higher values for  $E_b/N_0$ , where relatively low noise levels will cause few errors. A theoretical curve for BER is illustrated in Figure 20 for 4-ary FSK with no forward error correction (FEC) coding in a channel with added white Gaussian noise [22].

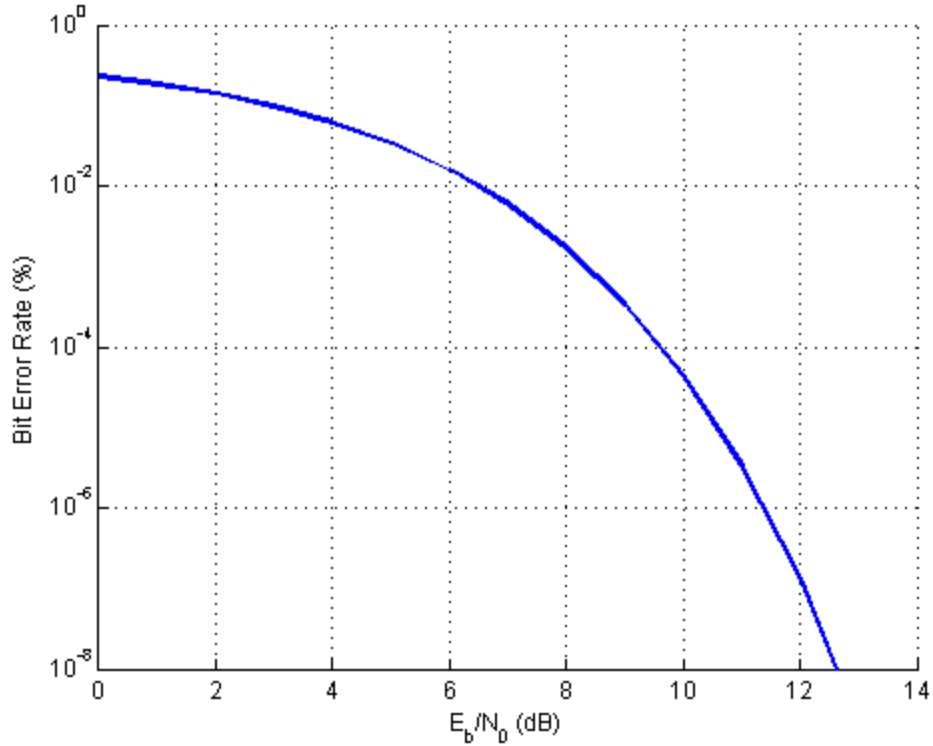


Figure 20. Theoretical BER for 4-ary FSK with no FEC in a channel with added white Gaussian noise [22].



## V. SIMULATIONS

In order to characterize the performance of bandwidth scaling and frequency multiplexing in various source-receiver geometries, we simulate the modulation, transmission, reception and demodulation of a signal through a multipath-induced fading channel. To illustrate these characteristics, and for computational efficiency, several simplifications and assumptions are made. The aim of these assumptions is to create a frequency-independent channel model and examine what happens to performance in the narrowband in response to the effects of the fading channel, source-receiver geometry, and pulse duration.

The simulated signal consists of only one pulse train of 4-ary FSK centered at 45 kHz, rather than the entire bandwidth-scaled or frequency-multiplexed multi-channel MFSK signal. Faithfully representing a broadband signal such as multi-channel MFSK would involve taking into account frequency-dependent effects on transmission loss. As discussed in Chapter II, due to the wideband distortion introduced by the ocean, these effects vary by tens of decibels from one edge of the signal's bandwidth to the other, and would thus present a significant degree of complexity to the model. Furthermore, the relative effects of the fading channel, source-receiver geometry, and pulse duration on the performance of the modulation schemes can still be illustrated with a single pulse train of 4-ary FSK.

We next make the assumption that the frequency-dependent transmission loss is constant across the bandwidth of the 4-ary FSK pulse train. At its narrowest for Seastar, the bandwidth of a single 4-ary FSK pulse train is 160 Hz, and at its widest, as in the case of bandwidth scaling, the bandwidth is 640 Hz. To show that the difference in transmission loss across these bandwidths is negligible, we treat the widest band possible, and accept the greatest variation in transmission loss with frequency. The difference between the uppermost and lowermost carrier frequencies in the 4-ary FSK pulse train is 480 Hz for bandwidth scaling. For comparison, we determine the transmission loss at the extremities of this 480 Hz band. As an added verification of the assumption of constant transmission loss, we perform this comparison for bands centered at 35.080 kHz and

54.920 kHz. The results, determined by both the Bellhop model and (2.27), are presented in Table 3, and indicate that the change in transmission loss with frequency is negligible for a single pulse train of 4-ary FSK for the case of the widest possible bandwidth. It follows that the transmission loss may be considered constant with frequency for narrower bandwidths.

	TL (Bellhop)		TL (Francois & Garrison, Cylindrical Spreading)	
Frequency (Hz)	Loss (dB)	Difference (dB)	Loss (dB)	Difference (dB)
34840	29.5151	0.0531	30.3861	0.0861
35320	29.5683		30.4722	
54680	31.6289	0.0467	34.5552	0.1132
55160	31.6756		34.6684	

Table 3. Transmission loss at the uppermost and lowermost carrier frequencies for a 4-ary FSK pulse train of bandwidth 640 Hz.

From the environmental parameters defined in Table 1, the RMS roughness of the surface is zero. We further assume that the source and receiver are stationary, allowing us to neglect Doppler spreading of the signal. No additional phase shifts are introduced beyond those introduced by the rays' interactions with the boundaries, and the frequency response of the transmitter and receiver are assumed to be flat.

#### A. BANDWIDTH SCALING

In this section, we consider two pulse durations—6.25 ms and 12.5 ms—that are associated with the bandwidth scaling implementation of multi-channel MFSK. Channel simulations are run for each of these pulse durations for source-receiver depths of 5 m, 50 m, 100 m, 150 m and 200 m, over ranges between 50 and 500 m. For both pulse durations, a small number of errors are observed only in the case where the source-receiver depth was 5 m, and only between ranges of 50 and 60 m. These results are shown in Figure 21. Thus, for this particular shallow source-receiver geometry and noise-free environment, ISI due to multipath spread appears to be an issue at short ranges.

Errors are not observed for the other four source-receiver depths, and no errors are observed in any of the depth configurations beyond a range of 60 m. Results from all simulations are presented in Appendix A.

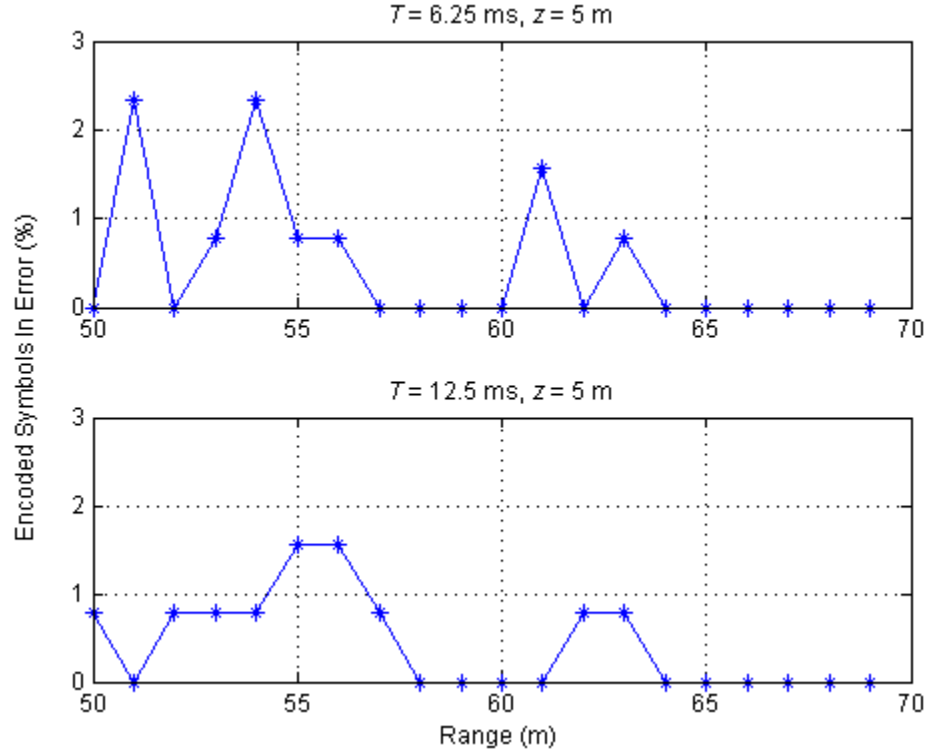


Figure 21. The percentage of encoded symbols received in error are shown for the pulse durations associated with bandwidth scaling at a source-receiver depth of  $z = 5 \text{ m}$  and for ranges between 50 and 70 m.

While errors are observed only in limited simulated cases, it is possible to predict the presence of ISI based on the times of arrivals of the multipath arrivals. By measuring the time, in symbols, between the start of the direct-path arrival and the start of the next multipath, we obtain a normalized time difference of arrival between these two paths. This normalized time difference of arrival is, in a sense, a measure of the “distance” in time between two symbols. We consider only these multipath arrivals for this comparison, as their amplitudes are the greatest of the multipath arrivals. The normalized time difference of arrival is given by:

$$\Delta t_N = \frac{t_1 - t_0}{T} \quad (5.1)$$

where  $t_0$  and  $t_1$  are the arrival times, in seconds, of the direct path and the next multipath arrivals, respectively, and  $T$  is the pulse duration, in seconds per pulse. Thus, (5.1) describes how many pulses away in time the next multipath arrival is from the direct path arrival. For  $\Delta t_N < 1$ , the direct-path pulse and next multipath pulse overlap, and for  $\Delta t_N > 1$ , the multipath symbol is interfering with a subsequent pulse other than the first. As an example, in the case where  $\Delta t_N = 1$ , the next multipath pulse begins just as the direct-path pulse ends, and is consequently interfering with the second pulse. Greater values for  $\Delta t_N$  thus correspond to an increased potential severity of ISI. It is important to emphasize that  $\Delta t_N$  is useful in evaluating the potential ISI, since its value does not take into account phase shifts; in essence, it is a metric of a worst-case scenario.

Figures 22 and 23 show the results of plotting (5.1) as a function of range for the five source-receiver depths and for each pulse duration. Plotted with (5.1) is a threshold that is meant to represent an arbitrary tolerance for a demodulator, and is for illustrative purposes only. The threshold is set for 0.75 symbols, but in reality, the practical threshold would depend on the characteristics of the receiver and its ability to demodulate the signal at that threshold. In Figure 22,  $\Delta t_N$  remains above the ISI tolerance threshold of 0.75 symbols for all source-receiver depths except for  $z = 5$  m and  $z = 200$  m, where the transmitter is only five meters away from the surface and bottom, respectively. Thus, in terms of time difference of arrival, bandwidth scaling with a 6.25 ms pulse duration would make the signal susceptible to ISI at all ranges for source-receiver geometries located at depths of 50 m, 100 m and 150 m.

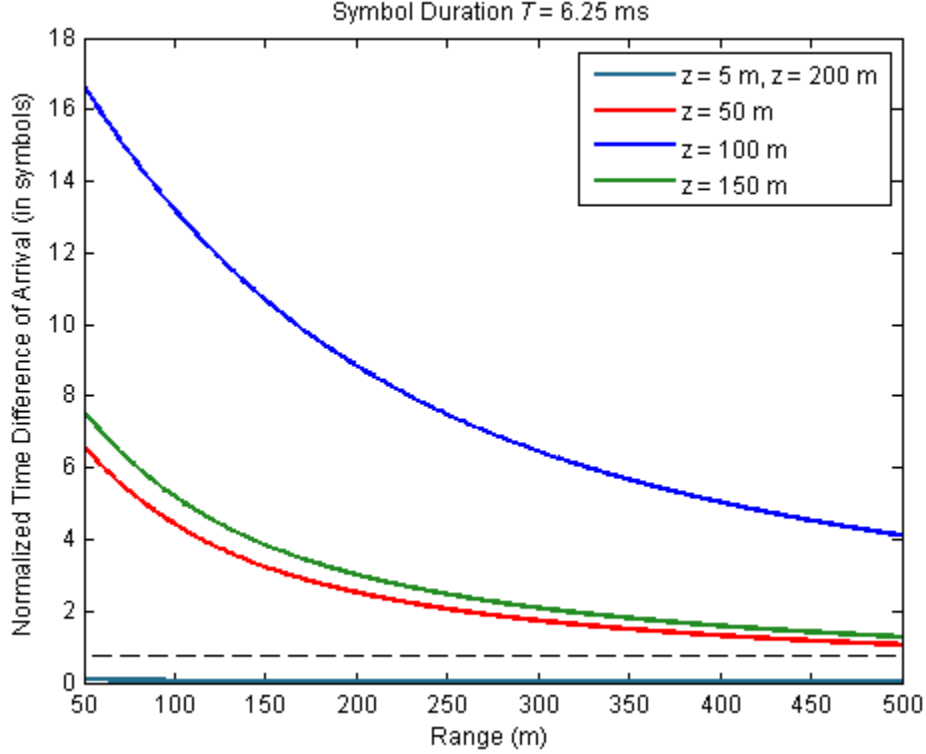


Figure 22. Normalized time difference of arrival between the direct path and next multipath arrivals for a signal with a pulse duration of 6.25 ms.

In Figure 23,  $\Delta t_N$  remains above the threshold at all ranges for a source-receiver depth of  $z = 100$  m. For  $z = 50$  m and  $z = 150$  m,  $\Delta t_N$  remains above the threshold at ranges between 50 and 350 m and 50 and 425 m, respectively. Thus, in terms of time difference of arrival, frequency multiplexing with a 12.5 ms pulse duration is susceptible to ISI at these ranges. For  $z = 5$  m and  $z = 200$  m,  $\Delta t_N$  is below the threshold for all ranges, and is not susceptible to ISI.

For both pulse durations, the normalized time difference of arrival  $\Delta t_N$  is highest at 50 m and lowest at 500 m. Furthermore, the pulse duration is inversely related to  $\Delta t_N$ : shortening the pulse duration increases  $\Delta t_N$ , and vice versa. We conclude that ISI is more likely to occur at shorter ranges than at longer ranges, and for shorter pulse durations than for longer pulse durations.

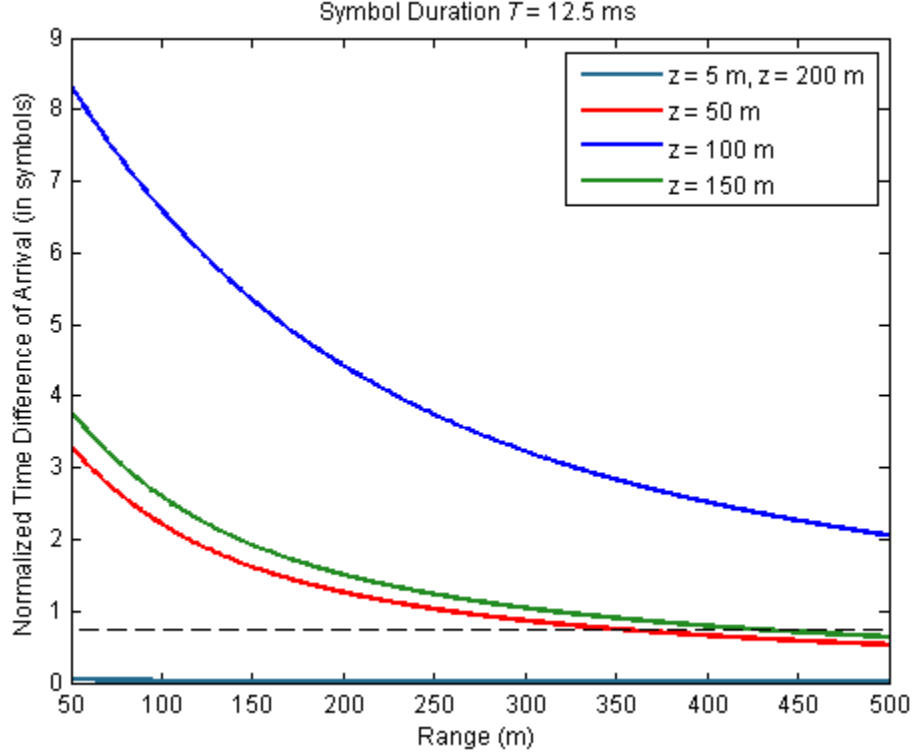


Figure 23. Normalized time difference of arrival between the direct path and next multipath arrivals for a signal with a pulse duration of 12.5 ms.

According to Figures 22 and 23 and the small values for  $\Delta t_N$  across all ranges for  $z = 5$  m and  $z = 200$  m, we should not expect ISI to occur, since for these source-receiver depths, the next multipath arrival is nearly synchronous with the direct-path arrival. However, this expectation directly contradicts the results presented in Figure 21, where errors did occur only at a source-receiver depth of 5 m. Upon closer examination of these signals' characteristics, we find that the amplitude of the next multipath signal is almost as strong as the direct-path signal. Figure 24 shows that the difference in sound pressure level (SPL) between the direct path and next multipath signal is extremely small for  $z = 5$  m and  $z = 200$  m, and much larger for the other source-receiver depths. Thus, despite  $\Delta t_N$  having the smallest values for  $z = 5$  m and  $z = 200$  m, the SPL of the next multipath arrival for these source-receiver depths is also the greatest, and is significant enough to cause ISI.

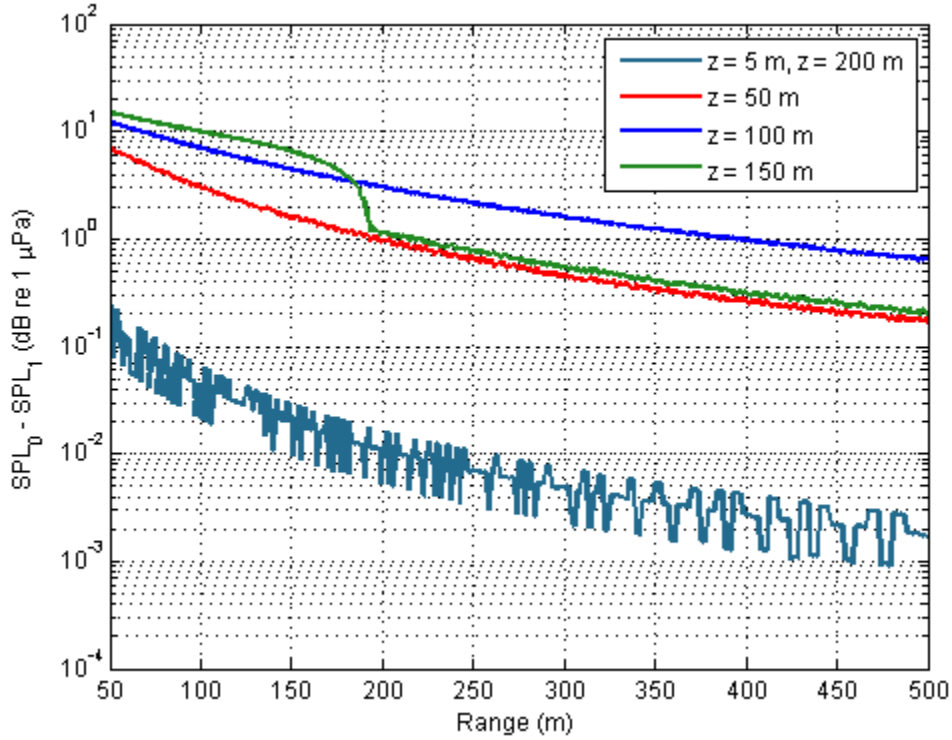


Figure 24. Difference in SPL between the direct-path signal and the next multipath.

## B. FREQUENCY MULTIPLEXING

In this section, we consider durations of 25 ms and 50 ms for pulses associated with the frequency-multiplexing implementation of multi-channel MFSK. Like the bandwidth scaling simulations, channel simulations are performed for each of these pulse durations for source-receiver depths of 5 m, 50 m, 100 m, 150 m and 200 m, at ranges between 50 and 500 m. For both pulse durations, fewer errors than the bandwidth scaling simulations are observed in the case where the source-receiver depth was 5 m. These results are shown in Figure 25. Thus, for this particular shallow source-receiver geometry and noise-free environment, ISI due to multipath propagation is still a factor at short ranges, but to a lesser degree. Errors are not observed for the other four source-receiver depths, and errors are not observed in any of the depth configurations beyond a range of 60 m. Results from all simulations are presented in Appendix A.

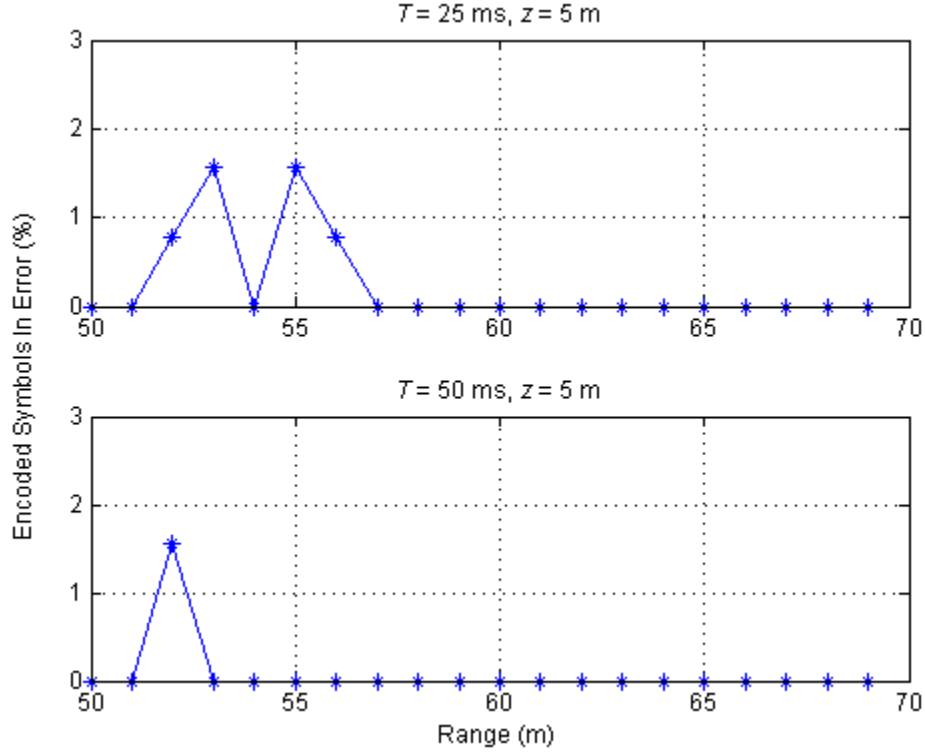


Figure 25. The percentage of encoded symbols received in error are shown for the pulse durations associated with frequency multiplexing at a source-receiver depth of  $z = 5 \text{ m}$  and for ranges between 50 and 70 m.

Figures 26 and 27 show the results of plotting (5.1), as it was plotted in Figures 22 and 23, but with the frequency-multiplexing pulse durations instead. Plotted with (5.1) is the same threshold of 0.75 symbols. In Figure 26,  $\Delta t_N$  remains above the threshold at all ranges for a source-receiver depth of  $z = 100 \text{ m}$ . For  $z = 50 \text{ m}$  and  $z = 150 \text{ m}$ ,  $\Delta t_N$  remains above the threshold at ranges between 50 and 164 m and 50 and 201 m, respectively. Thus, in terms of time difference of arrival, frequency multiplexing with a 25 ms pulse duration renders the signal susceptible to ISI at these ranges. For  $z = 5 \text{ m}$  and  $z = 200 \text{ m}$ ,  $\Delta t_N$  is below the threshold for all ranges, and the signal is not vulnerable to ISI.



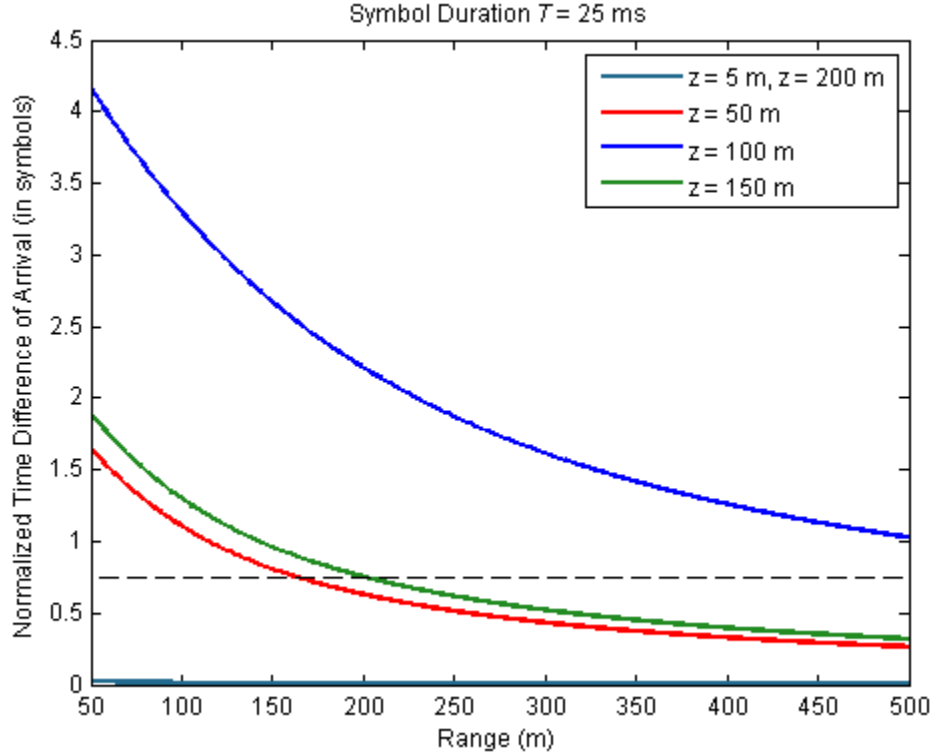


Figure 26. Normalized time difference of arrival between the direct-path and next multipath arrivals for a signal with a pulse duration of 25 ms.

In Figure 27,  $\Delta t_N$  falls below the threshold for a source-receiver depth of  $z = 100$  m at a range of 327 m. For  $z = 50$  m and  $z = 150$  m,  $\Delta t_N$  is almost completely below the threshold, but is above the threshold at ranges between 50 and 61 m and 50 and 80 m, respectively. Thus, in terms of time difference of arrival, frequency multiplexing with a 25 ms pulse duration is susceptible to ISI at these ranges. For  $z = 5$  m and  $z = 200$  m,  $\Delta t_N$  is below the threshold for all ranges, and the signal is not vulnerable to ISI.

For both pulse durations, the normalized time difference of arrival  $\Delta t_N$  is highest at 50 m and lowest at 500 m, as was the case for the bandwidth scaling pulse durations. The same inverse relationship between pulse duration and  $\Delta t_N$  holds, as well, meaning that ISI is also more likely to occur at shorter ranges than at longer ranges, and for shorter pulse durations than for longer pulse durations.

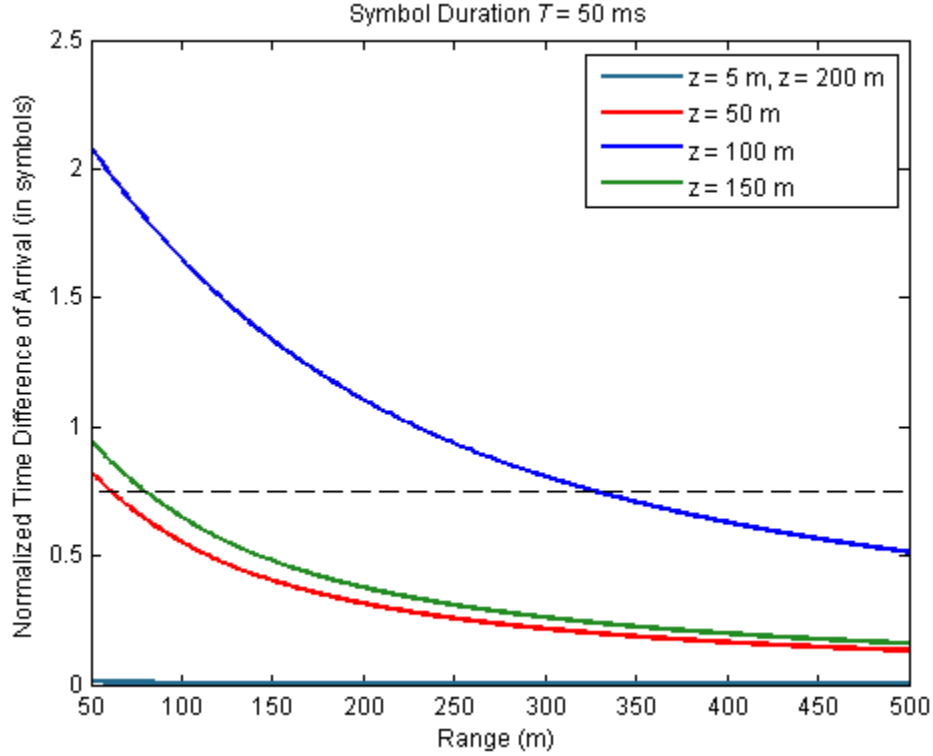


Figure 27. Normalized time difference of arrival between the direct-path and next multipath arrivals for a signal with a pulse duration of 50 ms.

As with the bandwidth scaling simulations, errors occurred during simulations at short-ranges for  $z = 5$  m. Once again, the primary contribution to these errors is the small difference in sound pressure level between the direct path and next multipath, shown in Figure 24. Despite  $\Delta t_N$  having the smallest values for  $z = 5$  m and  $z = 200$  m, the SPL of the next multipath arrival for these source-receiver depths is similar to that of the direct path, and is significant enough to cause ISI.

A comparison between simulations for the four pulse durations is given in Figure 28 and Table 4. This comparison shows that longer pulse durations produce fewer errors during demodulation, which confirms the prediction that was made by examining time differences of arrival (Figures 22, 23, 26 and 27) that smaller values for  $\Delta t_N$  lead to less ISI. Indeed, as illustrated by these figures, one way to decrease  $\Delta t_N$  is to increase the pulse duration.

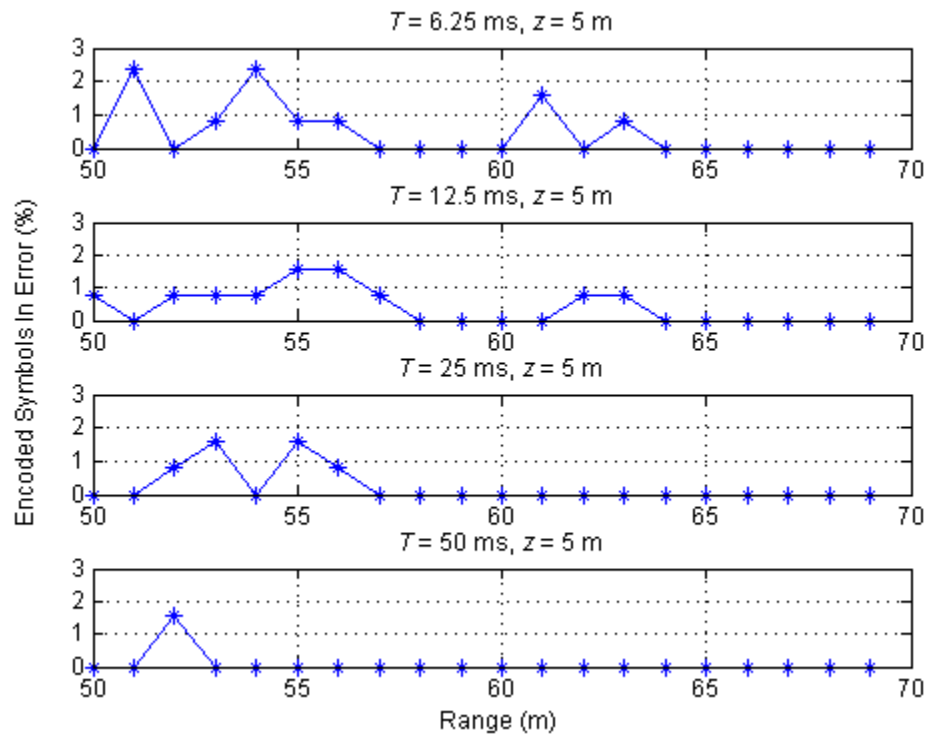


Figure 28. The percentage of encoded symbols received in error are shown for all four pulse durations at a source-receiver depth of  $z = 5$  m and for ranges between 50 and 70 m.

Pulse Duration (ms)	Total Errors
6.25	12
12.5	11
25	6
50	2

Table 4. Total of encoded symbols received in error for each pulse duration at a source-receiver depth of  $z = 5$  m and for ranges between 50 and 70 m.

THIS PAGE INTENTIONALLY LEFT BLANK

## VI. CONCLUSIONS

### A. FINDINGS

The simulations reported in Chapter V give insight into the relative performance of candidate implementations of multi-channel MFSK. While these results are too preliminary to be used for final design decisions, some general trends are evident that should inform the implementation of multi-channel MFSK.

Simulations in a noise-free environment yielded few errors for all pulse durations and geometries. However, lengthening the pulse duration decreases the time difference of arrival between the direct-path and next multipath arrivals, and reduces the potential for ISI. Furthermore, because the time difference of arrival decreases as range increases, the potential for ISI also decreases with greater distance between source and receiver.

The demonstrated relationship between pulse duration and time difference of arrival gives support to the frequency multiplexing implementation of multi-channel MFSK over the bandwidth scaling implementation. Consider a frequency-multiplexed implementation with four bands of multi-channel MFSK having a pulse duration of 50 ms. This implementation would have the same data rate as a bandwidth-scaled multi-channel MFSK signal with a pulse duration of 12.5 ms. The frequency multiplexing implementation is the preferable implementation, as it offers the same improved data rate of a bandwidth-scaled signal, but with the added benefit of having a longer pulse duration, thus making it more immune to multipath spread and less susceptible to ISI.

Apart from ISI, due to the high acoustic frequencies at which all the candidate implementations would operate, the single greatest cause of signal degradation is frequency and range dependent transmission loss and the presence of noise in the channel. As discussed in Chapter II, the idea of a high-frequency acoustic network must be limited to short-range applications, since, in a noisy environment, the power of the received signal may be overwhelmed by the power of the noise. The most challenging obstacle to short-range, high-frequency underwater acoustic communications is overcoming the effects of transmission loss and noise on the wideband signal.

## **B. RECOMMENDATIONS FOR FUTURE WORK**

Based on the simulation results, we recommend that steps be taken to implement on Seastar modems the frequency-multiplexed version of multi-channel MFSK. While this implementation will require more processing during demodulation than the bandwidth-scaled multi-channel MFSK signal, the penalty paid is small compared to the deleterious effects of ISI.

Evaluation of the candidate implementations of multi-channel MFSK would be improved through modeling the wideband multi-channel versions of the signals, rather than just a single pulse train of MFSK. While the single pulse train is useful for illustrative purposes and can give us insight as to what may be expected to happen to the wideband multi-channel MFSK signal, an accurate characterization of the channel's effects on the signal cannot be obtained until the full signal is propagated through a realistic channel model. Such a model would ideally be frequency-dependent, phase-coherent, and representative of the statistical characteristics of the channel boundaries at the surface and bottom.

The design of the demodulator may also be improved by implementing spectral equalization to help offset the frequency dependent effects of the channel. One way to implement such an equalizer would be to transmit a known wideband signal, analyze its received frequency spectrum to determine the effects of the channel on the signal, and adjust the amplitude weights of the FFT demodulator accordingly. Such a signal—a probe signal—could be transmitted before initiating the actual communications.

In addition to more accurately modeling the wideband implementations of multi-channel MFSK, the incorporation of FEC coding and interleaving to combat ISI would be realistic, as coding is routinely used aboard Seaweb modems [3]. Simulations using such coding would be more representative of what could be expected in actual testing and experimentation.

Beyond modeling, the various candidate implementations of multi-channel MFSK should be tested in the laboratory, and eventually at sea. Such testing reveals what is actually occurring to the signal as it propagates through the underwater acoustic communication channel.

## APPENDIX A. 4-ARY FSK SIMULATION RESULTS

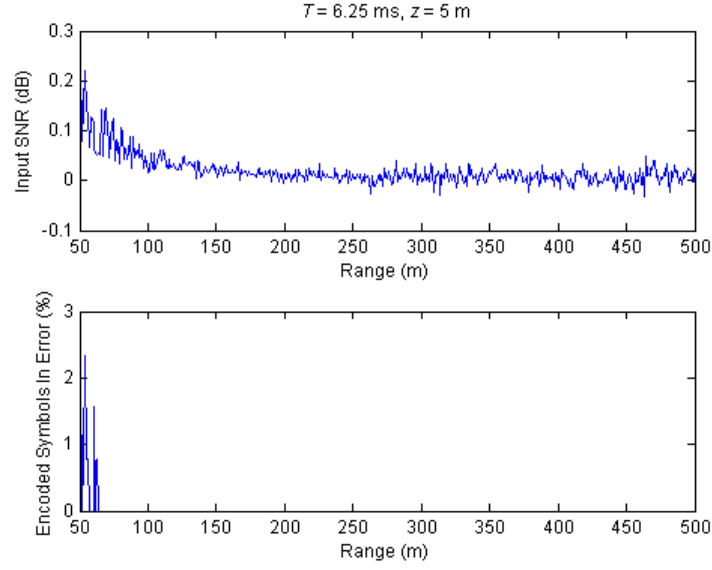


Figure 29. The input  $\text{SNR}_a$  and percentage of encoded symbols in error between 50 and 500 m for a signal with  $T = 6.25 \text{ ms}$  and a source and receiver located at  $z = 5 \text{ m}$ .

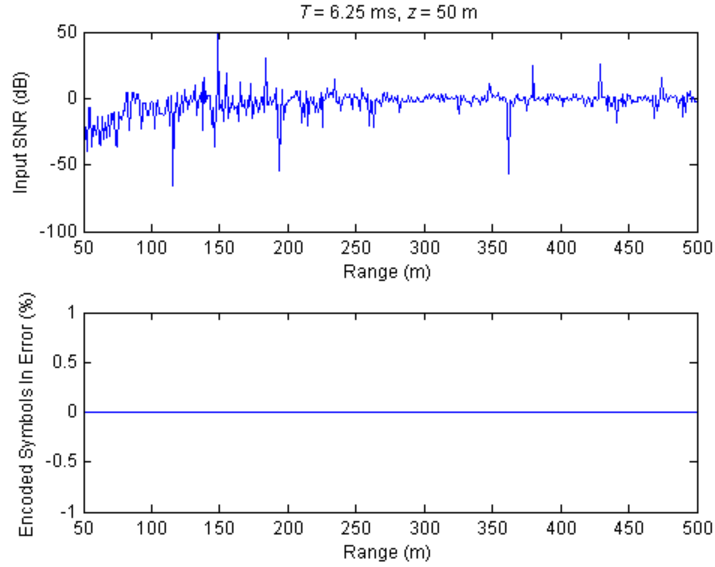


Figure 30. The input  $\text{SNR}_a$  and percentage of encoded symbols in error between 50 and 500 m for a signal with  $T = 6.25 \text{ ms}$  and a source and receiver located at  $z = 50 \text{ m}$ .

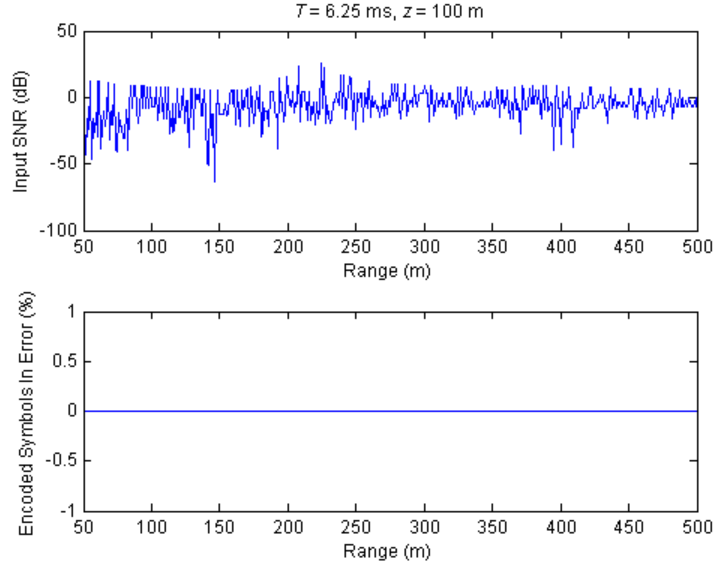


Figure 31. The input  $\text{SNR}_a$  and percentage of encoded symbols in error between 50 and 500 m for a signal with  $T = 6.25 \text{ ms}$  and a source and receiver located at  $z = 100 \text{ m}$ .

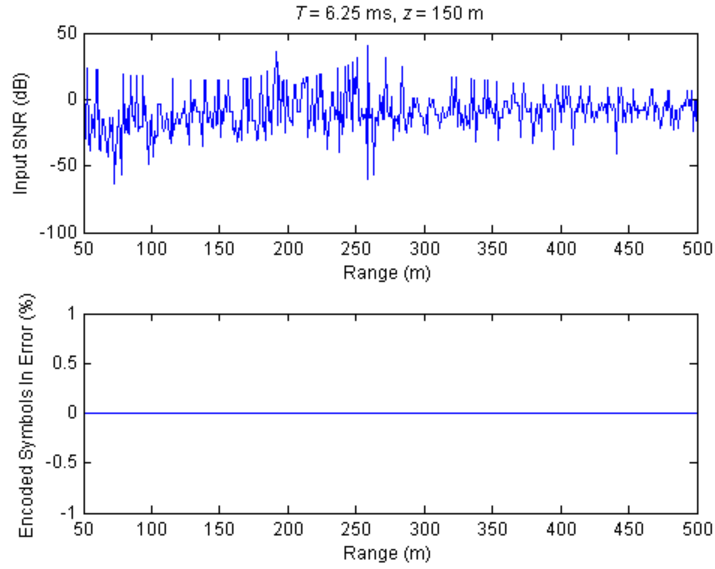


Figure 32. The input  $\text{SNR}_a$  and percentage of encoded symbols in error between 50 and 500 m for a signal with  $T = 6.25 \text{ ms}$  and a source and receiver located at  $z = 150 \text{ m}$ .



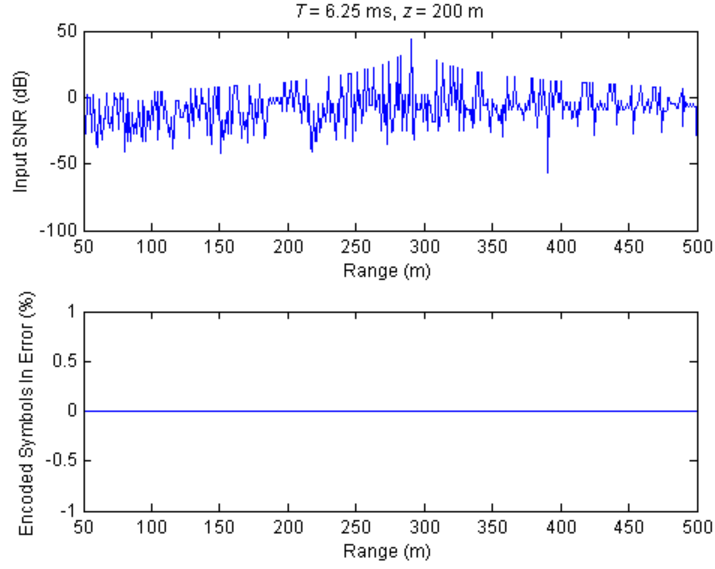


Figure 33. The input  $\text{SNR}_a$  and percentage of encoded symbols in error between 50 and 500 m for a signal with  $T = 6.25 \text{ ms}$  and a source and receiver located at  $z = 200 \text{ m}$ .

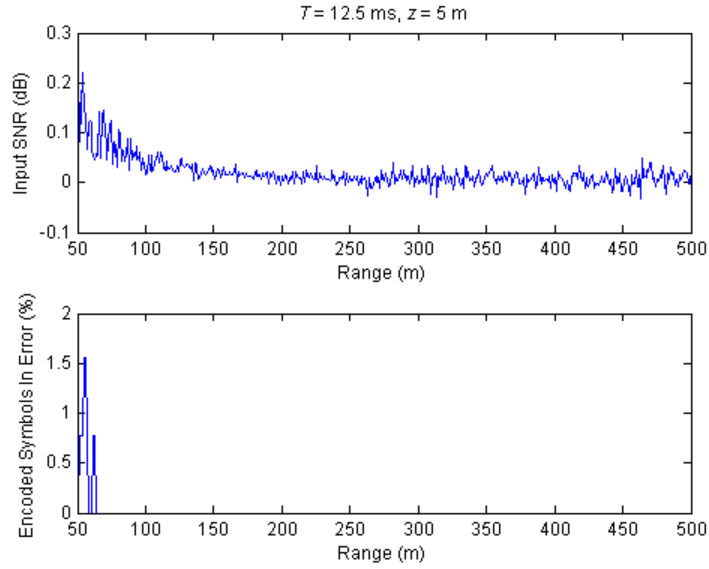


Figure 34. The input  $\text{SNR}_a$  and percentage of encoded symbols in error between 50 and 500 m for a signal with  $T = 12.5 \text{ ms}$  and a source and receiver located at  $z = 5 \text{ m}$ .

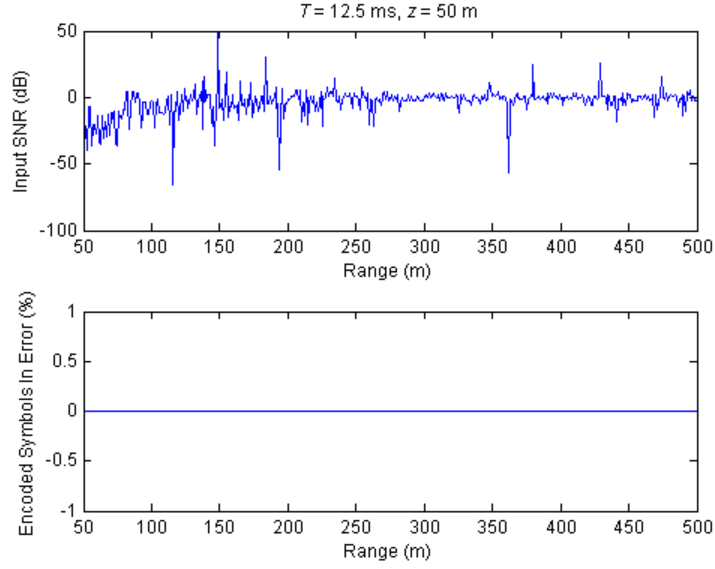


Figure 35. The input  $\text{SNR}_a$  and percentage of encoded symbols in error between 50 and 500 m for a signal with  $T = 12.5 \text{ ms}$  and a source and receiver located at  $z = 50 \text{ m}$ .

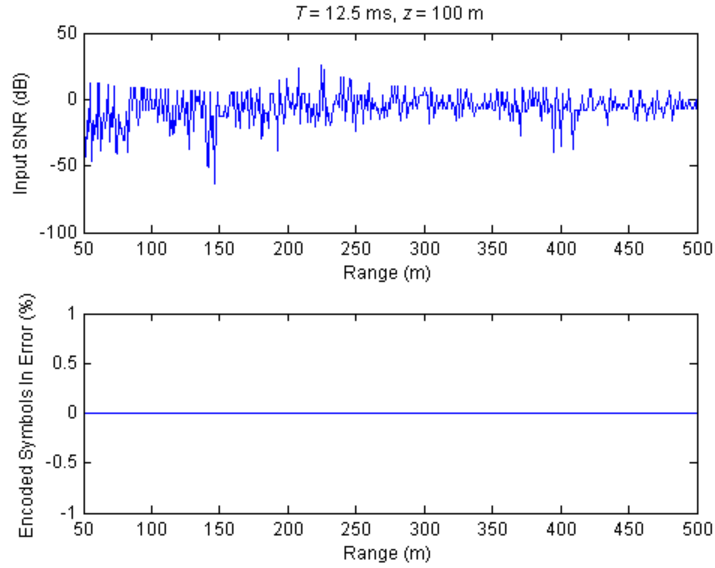


Figure 36. The input  $\text{SNR}_a$  and percentage of encoded symbols in error between 50 and 500 m for a signal with  $T = 12.5 \text{ ms}$  and a source and receiver located at  $z = 100 \text{ m}$ .

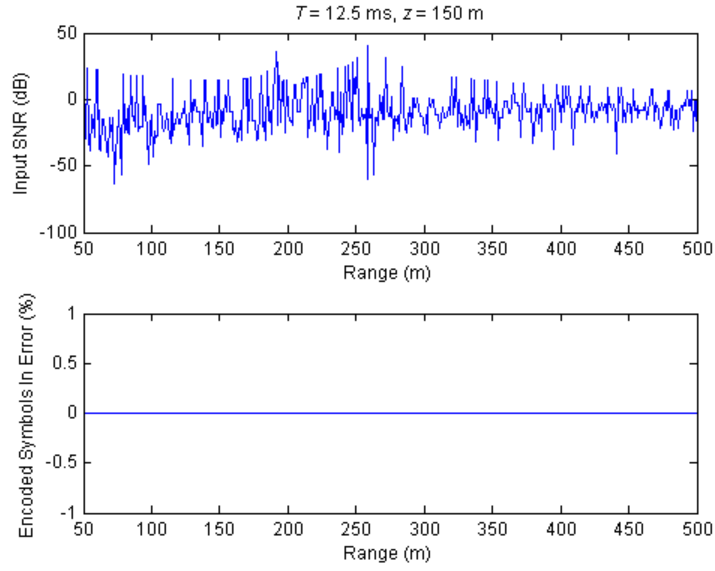


Figure 37. The input  $\text{SNR}_a$  and percentage of encoded symbols in error between 50 and 500 m for a signal with  $T = 12.5 \text{ ms}$  and a source and receiver located at  $z = 150 \text{ m}$ .

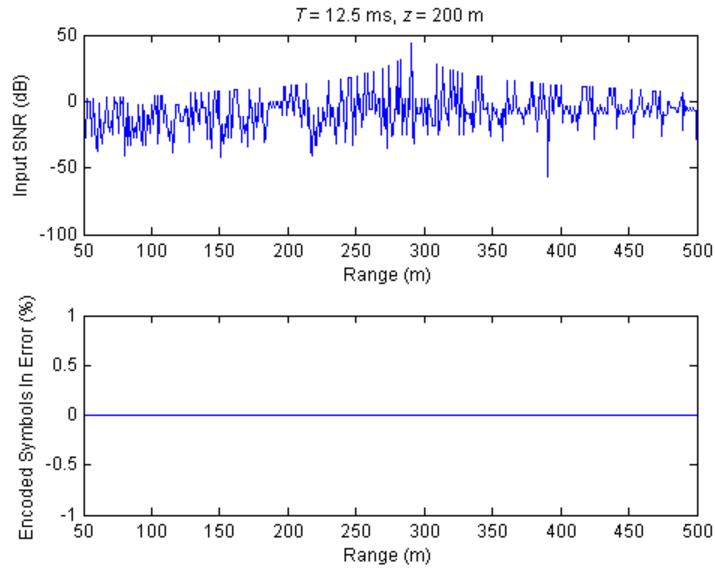


Figure 38. The input  $\text{SNR}_a$  and percentage of encoded symbols in error between 50 and 500 m for a signal with  $T = 12.5 \text{ ms}$  and a source and receiver located at  $z = 200 \text{ m}$ .

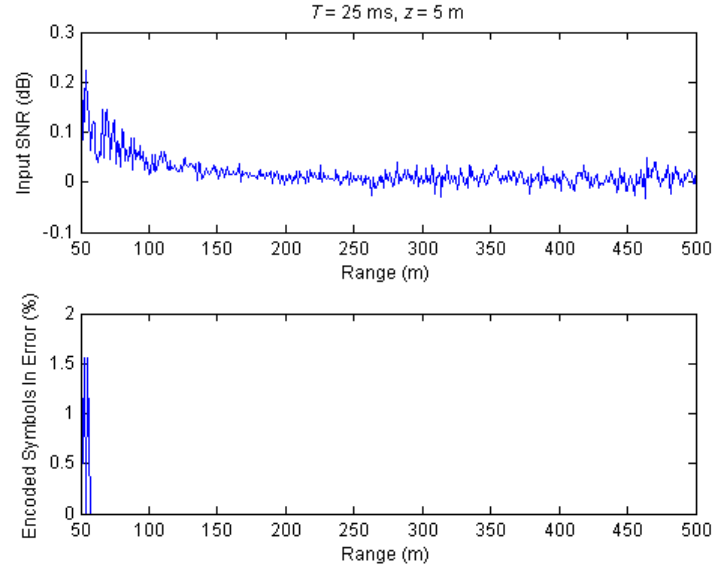


Figure 39. The input  $\text{SNR}_a$  and percentage of encoded symbols in error between 50 and 500 m for a signal with  $T = 25 \text{ ms}$  and a source and receiver located at  $z = 5 \text{ m}$ .

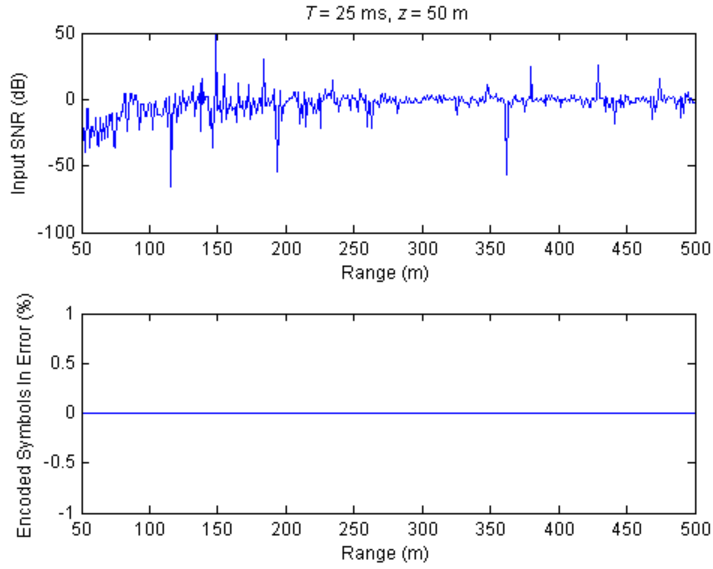


Figure 40. The input  $\text{SNR}_a$  and percentage of encoded symbols in error between 50 and 500 m for a signal with  $T = 25 \text{ ms}$  and a source and receiver located at  $z = 50 \text{ m}$ .

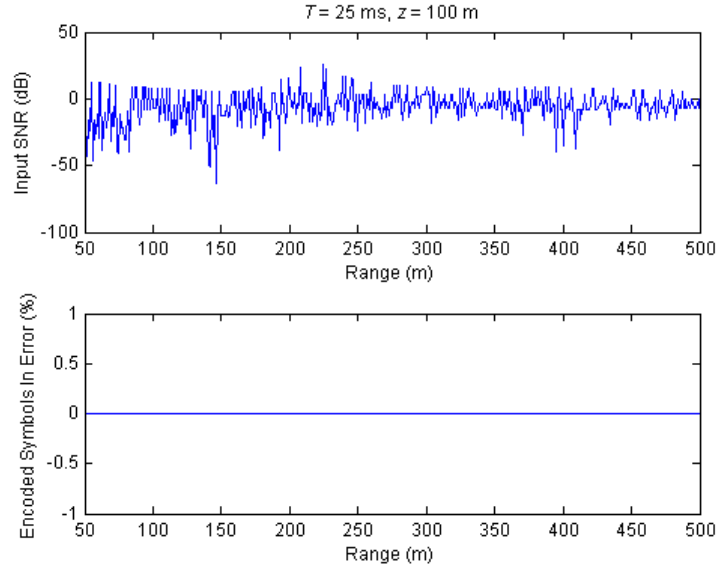


Figure 41. The input  $\text{SNR}_a$  and percentage of encoded symbols in error between 50 and 500 m for a signal with  $T = 25 \text{ ms}$  and a source and receiver located at  $z = 100 \text{ m}$ .

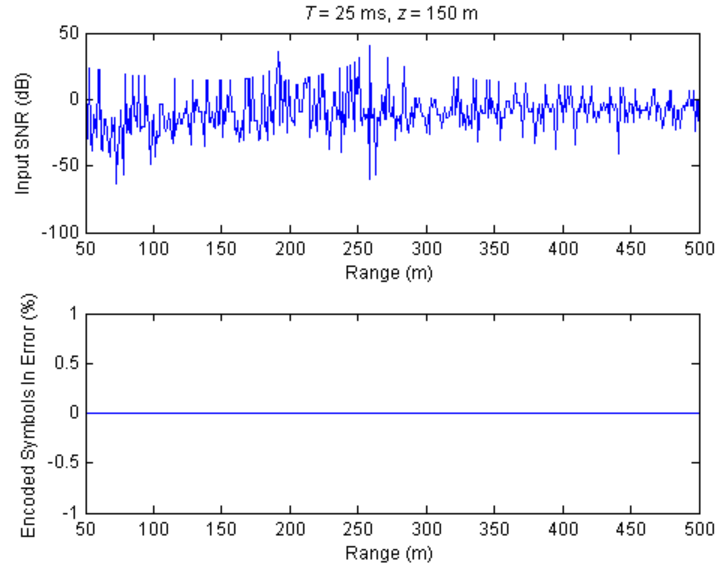


Figure 42. The input  $\text{SNR}_a$  and percentage of encoded symbols in error between 50 and 500 m for a signal with  $T = 25 \text{ ms}$  and a source and receiver located at  $z = 150 \text{ m}$ .

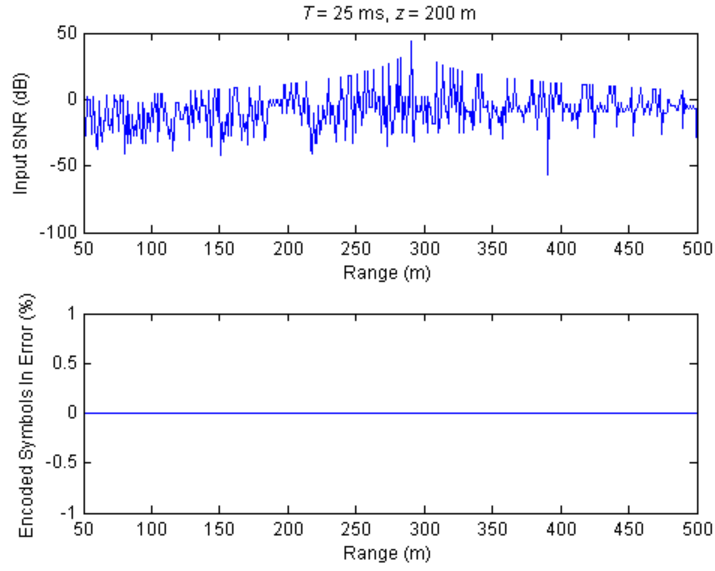


Figure 43. The input  $\text{SNR}_a$  and percentage of encoded symbols in error between 50 and 500 m for a signal with  $T = 25 \text{ ms}$  and a source and receiver located at  $z = 200 \text{ m}$ .

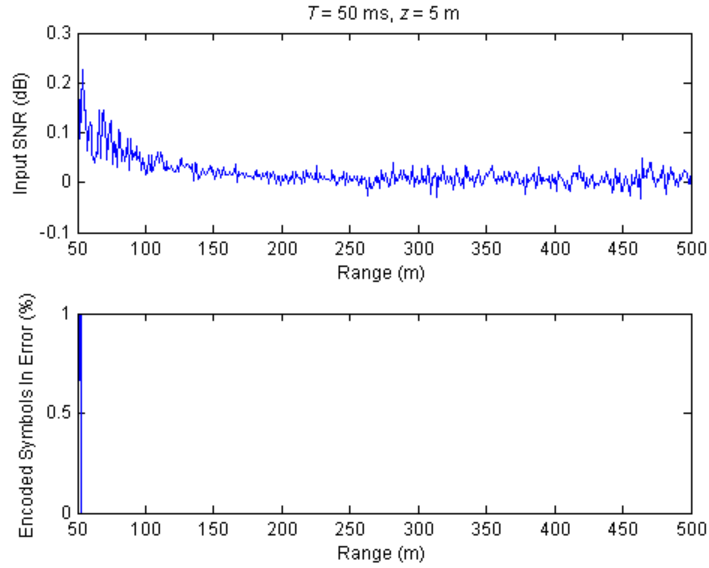


Figure 44. The input  $\text{SNR}_a$  and percentage of encoded symbols in error between 50 and 500 m for a signal with  $T = 50 \text{ ms}$  and a source and receiver located at  $z = 5 \text{ m}$ .

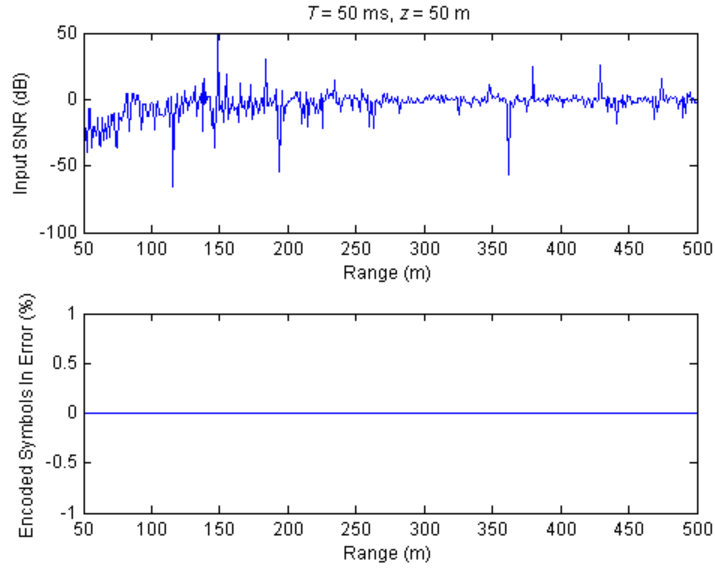


Figure 45. The input  $\text{SNR}_a$  and percentage of encoded symbols in error between 50 and 500 m for a signal with  $T = 50 \text{ ms}$  and a source and receiver located at  $z = 50 \text{ m}$ .

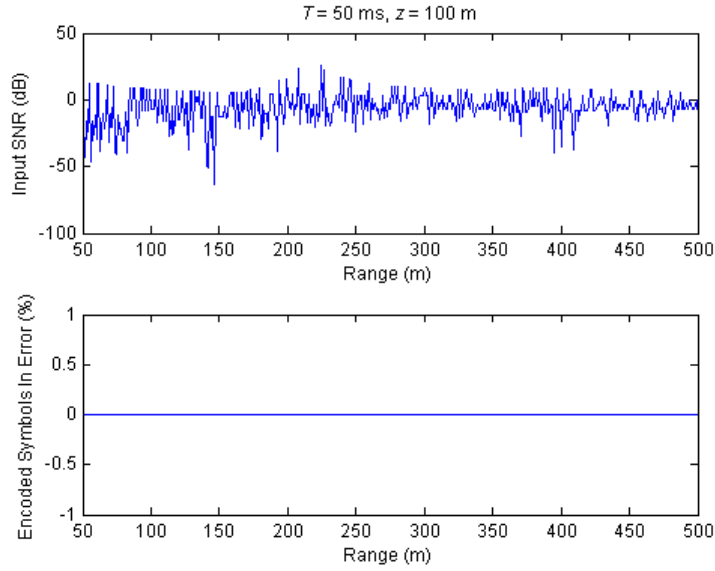


Figure 46. The input  $\text{SNR}_a$  and percentage of encoded symbols in error between 50 and 500 m for a signal with  $T = 50 \text{ ms}$  and a source and receiver located at  $z = 100 \text{ m}$ .

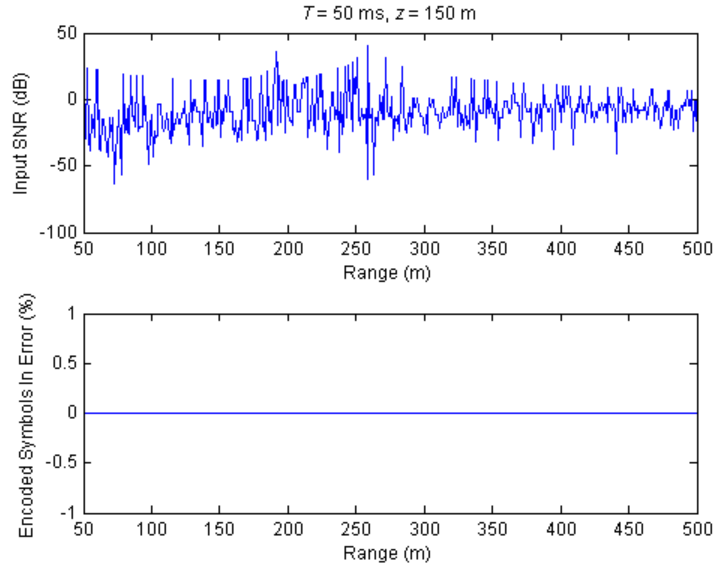


Figure 47. The input  $\text{SNR}_a$  and percentage of encoded symbols in error between 50 and 500 m for a signal with  $T = 50 \text{ ms}$  and a source and receiver located at  $z = 150 \text{ m}$ .

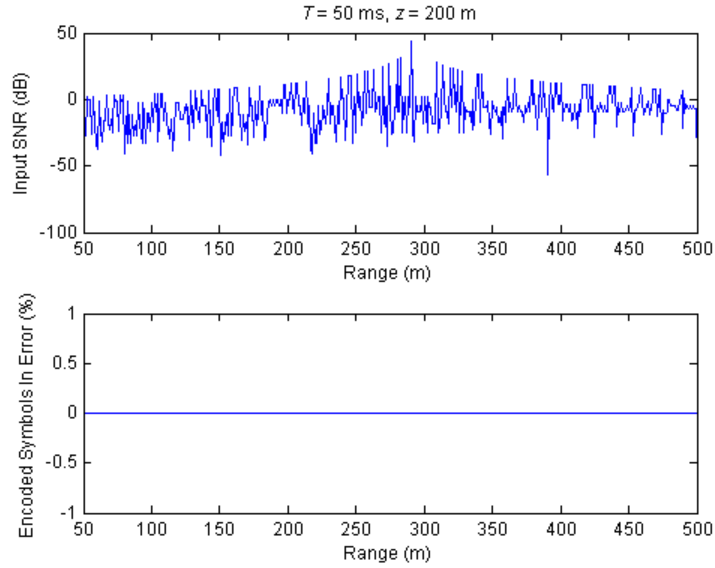


Figure 48. The input  $\text{SNR}_a$  and percentage of encoded symbols in error between 50 and 500 m for a signal with  $T = 50 \text{ ms}$  and a source and receiver located at  $z = 200 \text{ m}$ .



## APPENDIX B. 4-ARY FSK SIMULATION CODE

```
% This code modulates a 4-ary FSK signal, extracts channel response
data
% from Bounce-Bellhop Eigenray outputs, applies multipath arrivals to
% original signal, demodulates the received signal, and counts the
% errors.
% Functions Called:
% mfskcoder - Converts sequence of encoded symbols into a sequence of
%             channel symbols
% mfskdemod - Demodulates received signal into a sequence of received
%             channel symbols
% mfskdecoder - Converts sequence of received channel symbols into a
%              sequence of received encoded symbols
%
% William Jenkins
% Naval Postgraduate School, Monterey, California, May 2010

clear all
load impulsedata5
load wgnnoise

%% Signal Generation
encsym = 2; % Encoded Symbols per Channel Symbol
Tfactor = 1; % Time/Frequency Scaling Factor
Tsw = 0.025; % Seaweb Pulse Duration (sec)
fc = 45000; % Carrier Frequency (Hz)
% Arbitrary Sequence of Encoded Symbols
msg = [0 0 0 1 1 0 1 1 1 1 1 0 0 1 0 0 ...
       0 0 0 1 1 0 1 1 1 1 1 0 0 1 0 0];
msg = [msg msg msg msg];
N = length(msg)/2; % Number of Transmitted Channel Symbols
kn = mfskcoder(msg); % Symbol Vector

M = 2^encsym; % Number of Unique Channel Symbols
T = Tfactor*Tsw; % Pulse Duration (sec)
fs = 4*(fc+3/T); % Sampling Frequency (Hz)
Ts = 1/fs; % Sampling Period (sec)
T0 = floor(T/Ts);
t = Ts*(0:(T0-1));
tvec = Ts*(0:N*length(t)-1); % Time Vector
A = 1; % Amplitude

freqM = kn/(2*T);
freqtx = kron(freqM,ones(1,T0)); % Transmitted Frequency Vector

% Transmitted Signal
sig = A*0.5*(exp(1i*2*pi*(fc+freqtx).*tvec)...
        +exp(-1i*2*pi*(fc+freqtx).*tvec));

% Loop over Source-Receiver Depths
% 1 >>> z = 5m
```

```

% 2 >>> z = 50m
% 3 >>> z = 100m
% 4 >>> z = 150m
% 5 >>> z = 200m
geom = [1 2 3 4 5];
for zzz = 1:length(geom)
    %% Multipath Arrival & Noise Addition
    Range = zeros(1,length(time));
    errors = zeros(1,length(time));
    percent = zeros(1,length(time));
    SNRdB = zeros(1,length(time));

    % Loop over Source-Receiver Ranges
    for nnn = 1:length(time)

        delay_ind = zeros(1,length(time{nnn,geom(zzz)}}));
        prx = zeros(1,length(Prx{nnn,geom(zzz)}}));
        phase = zeros(1,length(phaserad{nnn,geom(zzz)}}));
        % Synchronization with First Arrival:
        tvec = tvec+min(time{nnn,geom(zzz)});

        for dd = 1:length(time{nnn,geom(zzz)})
            if time{nnn,geom(zzz)}(dd) > max(tvec)
                delay_ind(1,dd) = 0;
                prx(1,dd) = 0;
                phase(1,dd) = 0;
            else
                delay_vec = find(tvec >= time{nnn,geom(zzz)}(dd),1);
                delay_ind(1,dd) = min(delay_vec);
                prx(1,dd) = Prx{nnn,geom(zzz)}(dd);
                phase(1,dd) = phaserad{nnn,geom(zzz)}(dd);
            end
        end
        clear delay_vec
        multi = zeros(length(time{nnn,geom(zzz)}),length(sig));

        for dd = 1:length(delay_ind)
            if delay_ind(dd) == 0
                multi(dd,:) = zeros(1,length(sig));
            else
                multi(dd,:) = [zeros(1,delay_ind(dd)-1)...
                    prx(dd)*0.5*(exp(1i*2*pi*(fc+freqtx(delay_ind(dd):...
                        length(freqtx))).*tvec(delay_ind(dd):length(tvec)))...
                    *exp(1i*phase(dd))+exp(-1i*2*pi*...
                        (fc+freqtx(delay_ind(dd):length(freqtx))).*tvec...
                        (delay_ind(dd):length(tvec)))*exp(-1i*phase(dd)))]];
            end
        end

        sigrow = find(time{nnn,1}(:) == min(time{nnn,1}(:)));
        txsig = multi(sigrow,:);
        multi(sigrow,:) = [];

        noise = sum(multi);
    end
end

```

```

rxsig = txsig + noise;

%% Demodulation - FFT
% Demodulate received signal into received channel symbols:
knrx = mfskdemod(rxsig1,N,fs,fc,T,Tfactor);
% Demodulate received channel symbols into received encoded
% symbols:
[msgrx] = mfskdecoder(knrx);

%% Error Count

errvec = zeros(size(msg));
for mm = 1:length(msg)
    if msg(mm) == msgrx(mm)
        errvec(mm) = 0;
    else
        errvec(mm) = 1;
    end
end
% Total Encoded Symbols in Error:
errors(nnn) = sum(errvec);
% Percentage of Encoded Symbols in Error:
percent(nnn) = 100*errors(nnn)/length(msg);

% SNR at the Receiver (Input SNR)
% Average Power of the Transmitted Signal (Watts):
PIs = sum(abs(txsig.^2))/length(txsig);
% Average Power of the Noise (Multipath) (Watts):
PIn = sum(abs(noise.^2))/length(noise);
SNRdB(nnn) = 10*log10(PIs/PIn);

disp(['      Multipath SNR = ',num2str(SNRdB(nnn)),' dB'])
disp([num2str(errors(nnn)),...
      ' Errors Counted - Multipath'])
Range(nnn) = 49+nnn;
end
filename = ['Geometry',num2str(zzz),'_T',num2str(T*1000)];
save(filename,'errors','percent','SNRdB')
end

```

THIS PAGE INTENTIONALLY LEFT BLANK

## **APPENDIX C. DESCRIPTION OF THE BELLHOP UNDERWATER ACOUSTIC PROPAGATION MODEL**

The Bellhop underwater acoustic propagation modeling software used in this thesis is available as freeware from the Curtin Centre for Marine Science and Technology Web site. The software can be found on the “Products” page of their site: <http://cmst.curtin.edu.au/products/>

A link for more information is provided under the heading entitled “Underwater Acoustic Propagation Modeling Software (AcTUP). Following the link will bring the user to a page that describes the software. The current version is called “AcTUP V2.2L.”

Under the heading entitled “Downloads,” the user will find a link to download the software, and a link to download the user manual. Following the download link will bring the user to a form requesting end-user information. After completing and submitting the form, the software can be downloaded.

Installation should be completed with the aid of the user manual [8], as the manual’s instructions are helpful and accurate. The AcTUP GUI uses an independently developed acoustic toolbox for MATLAB, and following the manual ensures that the toolbox is placed in the correct directory for the GUI to access.

To run AcTUP once installation is complete, ensure the active MATLAB directory is correct, type “actup” in the command window, and hit enter/return. The AcTUP GUI will initialize. To begin configuring the model environment, select “Configure Environment & Propagation Models.” If the user has saved a previous run definition, it can now be loaded by selecting “Load Run Definition.”

To begin configuring an environment, select “Edit Environment.” For a range-independent environment, select “Edit Environment.” A window appears requesting the horizontal range for the environment; the default value is zero. After selecting “OK,” a window appears containing a list of layers being modeled. The user may add as many layers as desired. To edit each layer, select “Edit Layer.” A window appears requesting information about the layer, including whether the layer is a bottom half-space (yes or

no) and the RMS roughness of the top interface of the layer. Selecting “OK” after entering the desired values will bring the user to a new window in which physical properties of the layer are defined. The environment must be defined as a vector. For example, for an isospeed SSP of 1500 m/s, the compressional sound speed should be defined simply as [1500 1500]. The depth  $D$  between the sea surface and the bottom of the layer is similarly defined as [0  $D$ ]. Density, shear sound speed, compressional wave absorption, and shear wave absorption are similarly defined. For a varying SSP, simply increase the size of the vector of the environmental values. Keep in mind that the size of the vectors must be the same. Select “OK” to apply the environment definition, and repeat the process for additional layers. Select “OK” to close the window, and again to close the next window.

The next step is to define the propagation model parameters. Select “Edit Code-Independent Propagation Parameters.” Here the user defines a set of important values for the model. It is useful to enter a title unique to the parameters being used, especially when modeling over a variety of parameters or environments. A vector of frequencies can be defined, and the model will iterate over each frequency. Vectors of source and receiver depths may also be defined. In addition to iterating over depth, the model can iterate over range, enabling the user to define minimum and maximum ranges, as well as range resolution. To ensure that the model outputs can be easily located and identified, it is also useful to define a subdirectory in which the output files can be placed. A prefix for the output files is also desirable, and, like the title, should reflect the parameters of the model. Select “OK” to return to the main definition window.

Select “Edit Code-Dependent Propagation Parameters” to continue defining the model. Select “Bounce+Bellhop.” The first entry determines what kind of model will be run. “R” conducts a ray trace, “C” calculates transmission loss of a coherent signal, “I” calculates transmission loss of an incoherent signal, “S” calculates transmission loss of a semicoherent signal, “A” calculates the channel response, and an additional value that is not listed, “E,” calculates eigenrays. For the simulations in this thesis, “A” was selected. The next entry defines the beam type, and can either be set to Gaussian or geometric. The number of beams may be specified, along with the range of launch angles. After

selecting “OK,” a window appears asking if the user wishes to use a bathymetry file. To continue without a file, select “NO,” and then select “Exit Saving Changes.” This returns the user to the main definition window. At this point it is desirable to save the definitions that have just been set. Select “Save Run Definition” and save the definition file in the desired directory.

To run the model, select “Main Menu,” and then select “Run Current Model for ACTIVE Propagation Code.” The model will begin running. When the model has finished running, the user can select “Plotting Tools” to view the results. If “A” was chosen in the code-dependent definition window, select “Amplitude-delay for each ray path” to view a plot of the channel response. The abscissa is time, and the ordinate is the amplitude, expressed as a power ratio, between the received and transmitted signal.

To manipulate the output files with user-generated code, navigate to the directory ...\\AcTUP\\Output\\xyz\\Bounce+Bellhop\\, where xyz is the user-defined subdirectory. For the multipath analysis conducted in this thesis, data was extracted from the .ARR file type. The first line of the file specifies the frequency modeled and the number of ranges tested. The fourth line specifies the actual ranges modeled. Output data begins with line six. Here the number of amplitude-delay data points for a particular range is listed, followed by the data itself. The data is organized as follows: the first column is the amplitude; the second column is the phase (due to reflections); the third column is the time of arrival; the fourth and fifth columns are the launch angles; and the fifth and sixth columns specify the number of bottom and surface reflections a ray has encountered, respectively.

The code used to extract the data from the Bellhop output files is included in Appendix D.

THIS PAGE INTENTIONALLY LEFT BLANK



## APPENDIX D. DATA EXTRACTION CODE

```
% This code extracts data from the .arr amplitude-delay output files
% from Bellhop-Bounce and saves pertinent data in a .mat file.
%
% William Jenkins
% Naval Postgraduate School, Monterey, California, May 2010
clear all
addpath('..\THESIS\Seastar Bellhop Data')
d = [5, 50, 100, 150, 200]; % Depth of source and receiver (m)
f = 45;
for dd = 1:length(d)
file = ['..\THESIS\Seastar Bellhop Data\Final Analysis\Seastar_',...
        num2str(d(dd)), 'm_', int2str(f*1000), '.arr'];
fid = fopen(file);
NumRanges = textscan(fid, '%*f %*d %*d %*d', 1);
NumRanges = NumRanges{1,1};
for i = 1:6
    tline = fgetl(fid);
end
N = str2double(tline)+1;
% Assume Transmit Intensity of 1 W/m^2 @ 1 m.
pref = 1.0E-6; % Reference Pressure (Pa)
I0 = 1; % Intensity (Watts/m^2)
SL = 170.7 + 10*log(I0); % Source Level (dB re 1 uPa @ 1 m)
Ptx = pref*10^(SL/20); % Transmitted Acoustic Pressure (Pa)
for j = 1:NumRanges
    data{j,dd} = textscan(fid, '%f %f %f %f %f %d %d', N);
    Pratio{j,dd} = data{j,dd}{1,1}(1:N-1);
    Prx{j,dd} = Ptx*Pratio{j,dd};
    phasedeg{j,dd} = data{j,dd}{1,2}(1:N-1);
    phaserad{j,dd} = phasedeg{j,dd}*pi/180;
    time{j,dd} = data{j,dd}{1,3}(1:N-1);
    angle{j,dd} = horzcat(data{j,dd}{1,4}(1:N-1), ...
        data{j,dd}{1,5}(1:N-1));
    bounces_bot{j,dd} = data{j,dd}{1,6}(1:N-1);
    bounces_sur{j,dd} = data{j,dd}{1,7}(1:N-1);
    if j == 451
        N = 0;
    else
        N = data{j,dd}{1,1}(N)+1;
    end
end
end
save impulsedata5.mat Pratio Prx phasedeg phaserad time angle...
    bounces_bot bounces_sur pref I0 SL Ptx d
```

THIS PAGE INTENTIONALLY LEFT BLANK

## LIST OF REFERENCES

- [1] M. C. Goh, "Event-Driven Simulation and Analysis of an Underwater Acoustic Local Area Network," M.S. thesis, Dept. of Eng. Acoust., Naval Postgraduate School, Monterey, CA, 2010.
- [2] J. A. Rice, "Seaweb Underwater Networks," in *Proc. Acoust. 2005, Australian Acoust. Soc. Annu. Conf.*, Busselton, Australia, 2006.
- [3] J. A. Rice and D. Green, "Advances in Acoustic Communications and Undersea Networks," in *Proc. MAST 2008 Conf.*, Cadiz, Spain, 2008.
- [4] B. Kerstens, "A Study of the Seastar Underwater Acoustic Local Area Network Concept," M.S. thesis, Dept. of Eng. Acoust., Naval Postgraduate School, Monterey, CA, 2007.
- [5] K. F. Scussel, J. A. Rice and S. Merriam, "A new MFSK acoustic modem for operation in adverse underwater channels," in *Proc. Of the Oceans '97 Conf.*, Halifax, Canada, 1997.
- [6] C. D. McGillem and G.R. Cooper, *Continuous and Discrete Signal and System Analysis*, 3rd ed. Chicago, IL: Saunders College Publishing, 1991.
- [7] L. J. Ziomek, *Fundamentals of Acoustic Field Theory and Space-Time Signal Processing*. Boca Raton, FL: CRC Press, 1995.
- [8] A. L. Maggi and A. J. Duncan. (Accessed Feb. 2010). AcTUP v2.21a Acoustic Toolbox User-interface & Post-processor: Installation & User Guide. Curtin University of Technology, Centre for Marine Science & Technology. Perth, Australia. [Online]. Available: [http://cmst.curtin.edu.au/local/docs/products/actup\\_v2\\_21\\_installation\\_user\\_guide.pdf](http://cmst.curtin.edu.au/local/docs/products/actup_v2_21_installation_user_guide.pdf)
- [9] R. J. Urick, *Principles of Underwater Sound*, 3rd ed. Los Altos Hills, CA: Peninsula Publishing, 1983.
- [10] R. F. W. Coates, *Underwater Acoustic Systems*. New York: Halsted Press, 1989.
- [11] J. T. Hansen, "Link Budget Analysis for Undersea Acoustic Signaling," M.S. thesis, Dept. of Eng. Acoust., Naval Postgraduate School, Monterey, CA, 2002.
- [12] L. E. Kinsler, A. R. Frey, A. B. Coppens and J. V. Sanders, *Fundamentals of Acoustics*, 4th ed. New York: John Wiley & Sons, 2000.
- [13] K. Scussel and K. Amundsen. (Feb. 2009). Seastar Short-Range Modems, Transducer Performance Report. Teledyne Benthos. North Falmouth, MA. [Print].

- [14] O. B. Wilson, *Introduction to Theory and Design of Sonar Transducers*. Los Altos, CA: Peninsula Publishing, 1988.
- [15] C. Calnan. (Feb. 2006). DMOS – Bellhop Extension. DRDC Atlantic. Halifax, NS. [Print].
- [16] F. H. Fisher and V. P. Simmons, “Sound Absorption in Sea Water,” *J. Acoust. Soc. Am.*, vol. 62, no. 3, pp. 558–564, Sept. 1977.
- [17] R. E. Francois and G. R. Garrison, “Sound absorption based on ocean measurements: Part I: Pure water and magnesium sulfate contributions,” *J. Acoust. Soc. Am.*, vol. 72, no. 3, pp. 896–907, Sept. 1982.
- [18] R. E. Francois and G. R. Garrison, “Sound absorption based on ocean measurements: Part II: Boric acid contribution and equation for total absorption,” *J. Acoust. Soc. Am.*, vol. 72, no. 6, pp. 1879–1890, Dec. 1982.
- [19] J. O. Smith, III, *Physical Audio Signal Processing*. Stanford, CA: W3K Publishing, 2010.
- [20] G. M. Wenz, “Acoustic Ambient Noise in the Ocean: Spectra and Sources,” *J. Acoust. Soc. Am.*, vol. 34, no. 12, pp. 1936–1956, Dec. 1962.
- [21] W. W. K. Au and K. Banks, “The acoustics of the snapping shrimp *Synalpheus parneomeris* in Kaneohe Bay,” *J. Acoust. Soc. Am.*, vol. 103, no. 1, pp. 41–47, Jan. 1998.
- [22] J. G. Proakis, *Digital Communications*, 4th ed. New York: McGraw-Hill, 2001.
- [23] D. R. Lide, Ed., *CRC Handbook of Chemistry and Physics*, 90th ed. Boca Raton, FL: CRC Press, 2009.
- [24] D. Green. (Mar. 2009). Design Specifications, Seaweb Telesonar Header Packet. Teledyne Benthos. North Falmouth, MA. [Print].
- [25] H. P. E. Stern, S.A. Hahmoud and L.E. Stern, *Communication Systems Analysis and Design*. Upper Saddle River, NJ: Pearson Education, 2004.
- [26] J. G. Proakis and M. Salehi, *Communication Systems Engineering*, 2nd ed. Upper Saddle River, NJ: Pearson Prentice Hall, 2002.
- [27] W. Stallings, *Data and Computer Communications*, 8th ed. Upper Saddle River, NJ: Pearson Education, 2007.
- [28] L. E. Frenzel, Jr., *Principles of Electronic Communication Systems*, 3rd ed. New York: McGraw-Hill, 2008.

## INITIAL DISTRIBUTION LIST

1. Defense Technical Information Center  
Ft. Belvoir, Virginia
2. Dudley Knox Library  
Naval Postgraduate School  
Monterey, California
3. Joseph Rice  
Department of Physics  
Naval Postgraduate School  
Monterey, California
4. Lawrence Ziomek  
Department of Electrical and Computer Engineering  
Naval Postgraduate School  
Monterey, California
5. RADM (Ret.) Winford G. Ellis, USN  
Chair, Undersea Warfare  
Director, Undersea Warfare Research Center  
Naval Postgraduate School  
Monterey, California
6. Paul Gendron  
SPAWAR Systems Command Pacific  
San Diego, California
7. Dale Green  
Teledyne-Benthos  
Falmouth, Massachusetts
8. MAJ Meng Chong Goh  
Republic of Singapore Navy  
Naval Postgraduate School  
Monterey, California
9. LTJG Pongsakorn Sommai  
Royal Thai Navy  
Naval Postgraduate School  
Monterey, California

10. Chris Fletcher  
SPAWAR Systems Command Pacific  
San Diego, California
11. LCDR Bjørn Kerstens  
Royal Netherlands Navy
12. Roald Otnes  
Norwegian Defense Research Establishment  
Horten, Norway
13. Chad Spooner  
Naval Postgraduate School  
Monterey, California
14. Leroy Sverduk  
Office of Naval Research  
Arlington, Virginia
15. T.C. Yang  
Naval Research Laboratory  
Washington, DC
16. Jeff Schindall  
Naval Research Laboratory  
Washington, DC
17. Greg Vaughn  
Science Applications International Corporation  
Arlington, Virginia
18. ENS William F. Jenkins II, USN  
Naval Postgraduate School  
Monterey, California